Published in final edited form as:
Nature. 2017 July 05; 547(7661): 43–48. doi:10.1038/nature22995.

West Antarctic Ice Sheet retreat driven by Holocene warm water incursions

Claus-Dieter Hillenbrand[1,*], **James A. Smith**[1], **David A. Hodell**[2], **Mervyn Greaves**[2], **Christopher R. Poole**[3,4], **Sev Kender**[5,6], **Mark Williams**[3], **Thorbjørn Joest Andersen**[7], **Patrycja E. Jernas**[8], **Henry Elderfield**[2,†], **Johann P. Klages**[9], **Stephen J. Roberts**[1], **Karsten Gohl**[9], **Robert D. Larter**[1], and **Gerhard Kuhn**[9]

[1]British Antarctic Survey, High Cross, Madingley Road, Cambridge CB3 0ET, UK

[2]Department of Earth Sciences, Cambridge University, Downing Street, Cambridge CB2 3EQ, UK

[3]Department of Geology, University of Leicester, Leicester, LE1 7RH, UK

[4]Department of Earth Sciences, University College London, London WC1E 6BT, UK

[5]British Geological Survey, Keyworth, Nottingham, NG12 5GG, UK

[6]Camborne School of Mines, University of Exeter, Penryn, Cornwall TR10 9FE, UK

[7]Center for Permafrost (CENPERM), Department of Geosciences and Natural Resource Management, University of Copenhagen, 1350 Copenhagen K, Denmark

[8]Department of Geology, University of Tromsø - The Arctic University of Norway, N-9037 Tromsø, Norway

[9]Alfred-Wegener-Institut Helmholtz-Zentrum für Polar- und Meeresforschung, Department of Geosciences, Am Alten Hafen 26, D-27568 Bremerhaven, Germany

Abstract

Glaciological and oceanographic observations coupled with numerical models show that warm Circumpolar Deep Water (CDW) upwelling onto the West Antarctic continental shelf causes melting of the undersides of floating ice shelves. Because these ice shelves buttress glaciers feeding into them, their ocean-induced thinning is driving Antarctic ice-sheet loss today. Here we present the first multi-proxy data based reconstruction of variability in CDW inflow to the

[*]Correspondence and requests for materials should be addressed to C.-D.H. (hilc@bas.ac.uk).
[†]deceased

Author contributions C.-D.H. conceived the idea for the study and together with J.A.S., G.K. and R.D.L. wrote the manuscript. G.K., C.-D.H. and K.G. collected the PS69 sediment core and together with J.A.S., P.E.J. and J.P.K. the PS75 cores. C.-D.H., J.A.S. and S.J.R. developed the ^{14}C age models for the PS75 cores. R.D.L. designed Figure 1. T.J.A. conducted the ^{210}Pb measurements on the PS69 core and provided its age model. G.K., C.-D.H., J.A.S., J.P.K. and P.E.J. undertook the sedimentological analyses. D.H. measured stable isotopes on the foraminifer shells, while M.G. and H.E. analysed the trace metals. C.R.P., S.K. and M.W. analysed the foraminifer assemblages. All co-authors commented on the manuscript and provided input to its final version.

Author information Reprints and permissions information is available at www.nature.com/reprints. Readers are welcome to comment on the online version of the paper.

The authors declare no competing financial interests.

Europe PMC Funders Author Manuscripts

Amundsen Sea sector, the most vulnerable part of the West Antarctic Ice Sheet, during the last 11,000 years. The chemical composition of foraminifer shells and benthic foraminifer assemblages in marine sediments indicate that enhanced CDW upwelling, controlled by the latitudinal position of the Southern Hemisphere westerly winds, forced deglaciation of this sector both until 7,500 years ago, when an ice-shelf collapse may have caused rapid ice-sheet thinning further upstream, and since the 1940s. These results increase confidence in the predictive capability of current ice-sheet models.

Today ice discharge from glaciers flowing into the Amundsen Sea Embayment (ASE) (Fig. 1) is the main contributor to the negative mass balance of the West Antarctic Ice Sheet (WAIS) and global sea-level rise from Antarctica1. Rapid thinning, flow acceleration, and grounding-line retreat affecting ice streams and ice shelves in this region have increased since the early 1970s and contributed to global sea-level rise by, on average, ~0.23±0.02 mm/yr between 1992 and 20131–3. Recent modelling suggests that current ice loss of the Thwaites Glacier (Fig. 1), which rests on a bed that is well below sea level and slopes down into the interior of the ASE hinterland, will result in a (partial) WAIS collapse from as early as the 23rd century, thereby raising global sea level over centuries and millennia at rates ≥1 mm/yr (ref. 4). A similar study predicts that neighbouring Pine Island Glacier, which drains together with Thwaites Glacier into Pine Island Bay (PIB) in the eastern ASE (Fig. 1), will contribute ~3.5-10 mm to eustatic sea-level rise over the next two decades alone5. Depending on the future extent of atmospheric and oceanic warming, and the dominant processes of ice loss, Antarctica may contribute as much as 1 metre to global sea-level rise by the end of this century6.

Ocean-driven melting of the undersides of floating ice shelves buttressing the glaciers draining into the ASE has been identified as the main process responsible for the current mass loss. This melting is caused primarily by upwelling of relatively warm Circumpolar Deep Water (CDW) onto the continental shelf7–12. Inter-annual to inter-decadal changes in CDW upwelling onto the ASE shelf have been attributed to buoyancy changes9 and regional climate variability10. The latter is assumed to be controlled by latitudinal shifts in the Southern Hemisphere westerly winds (SHWW)11, possibly in response to the Southern Annular Mode and teleconnections to climate in the tropical Pacific12.

While West Antarctic ice cores provide high-resolution archives of atmospheric changes through the last glacial period to today13, satellite observations and *in situ* measurements of glaciological1–3 and oceanographic changes7,10 are restricted to the last ~30-40 years8,14. Until now, no data constrain CDW upwelling onto the inner ASE shelf prior to this time, and its role in driving centennial to millennial retreat of the WAIS remains unclear. This information, however, is crucial for verifying the reliability of the current generation of ice-sheet models which force WAIS deglaciation following the Last Glacial Maximum (LGM; 19-23 kyr BP) predominantly by ocean-induced melting15–17 and predict that this process will also drive future Antarctic ice loss in response to global warming18, at least during its initial phase6. Until now, simulations of ocean forcing have predominantly relied on estimates of deep-water temperatures derived from global climate models that are

Europe PMC Funders Author Manuscripts

constrained by far-field oceanic records from outside the Southern Ocean and its complex circulation system6,15–17.

Foraminifer shell chemistry and seawater

Here we present the first direct evidence for variations in CDW heat supply onto the ASE shelf during the last 10.4 kyr. We measured the magnesium/calcium (Mg/Ca) ratio of calcareous shells of the epifaunal to shallow infaunal benthic foraminifer species *Angulogerina angulosa* (Methods) in core PS75/160 recovered just offshore from Pine Island Glacier19 (Fig. 1). The Mg/Ca data are used as a proxy for bottom-water temperature20 and thus inflow of CDW onto the ASE shelf (Methods). The low-resolution Mg/Ca record of core PS75/160 is supported by a high-resolution stable carbon isotope ($\delta^{13}C$) dataset obtained from calcareous shells of *A. angulosa* and the planktic foraminifer species *Neogloboquadrina pachyderma* sinistral from the same site and site PS75/167, which is located just offshore from Thwaites Glacier (Fig. 1). We utilize the benthic $\delta^{13}C$ ratio as a proxy for the carbon isotope composition of the dissolved inorganic carbon ($\delta^{13}C_{DIC}$) of the ambient seawater and thus, as a tracer for its source water mass. We also measured $\delta^{13}C$ values of *A. angulosa* in modern sediments from site PS75/215 in PIB and on *N. pachyderma* sin. in recent sediments from site PS69/251 on the outer ASE shelf19,21 (Fig. 1).

Foraminiferal $\delta^{13}C$ records from marine sediments are influenced by water-mass circulation in addition to vital effects, biological productivity, air-sea exchange of carbon, or a combination of these factors22–28. We corrected the $\delta^{13}C$ data for species-inherent vital effects as follows: The $\delta^{13}C$ signal of *A. angulosa* is known to be on average 0.44-0.60 ‰ lower than the $\delta^{13}C_{DIC}$ of ambient seawater, but this offset varies regionally23. Mackensen24 analysed the carbon isotope composition of the epibenthic foraminifer genus *Cibicidoides* spp., a reliable recorder of bottom water $\delta^{13}C_{DIC}$, in core-top sediments from site PS2544 on the outer ASE shelf (Fig. 1). The measured $\delta^{13}C$ value of +0.63 ‰ overlaps with the $\delta^{13}C_{DIC}$ range of ~0.3 to 0.6 ‰ reported for CDW25,26 when the analytical errors for $\delta^{13}C$ measurements of seawater (±0.1 ‰) and foraminiferal calcite (±0.06 ‰) are taken into account24. In contrast, we measured a $\delta^{13}C$ ratio of -0.22 ‰ on *A. angulosa* from modern sediments at site PS75/215. Because both core sites are currently bathed by CDW7–11, we applied an offset correction of +0.85 ‰ to our benthic $\delta^{13}C$ data. Previous studies on *N. pachyderma* sin. shells from south of the Antarctic Polar Front27 and south of 70 °S (ref. 28), respectively, found a $\delta^{13}C$ offset of -1.0 ‰ between the shells and the ambient surface waters. Accordingly, we corrected our planktic $\delta^{13}C$ data by adding +1.0 ‰.

To evaluate the influence of past changes in biological productivity on the foraminiferal $\delta^{13}C$ down-core record, we measured barium/titanium (Ba/Ti) ratios of cores PS75/160 and PS75/167 (Fig. 2, Extended Data Fig. 5) as the most reliable palaeoproductivity proxy in Antarctic continental margin sediments29. Furthermore, we examined the benthic foraminifer assemblages in sediments of core PS75/160 for evidence of environmental changes, especially whether an ice shelf covered PIB from ~12.3-11.2 kyr BP onwards30,31. Ice-shelf cover would have reduced the foraminiferal $\delta^{13}C$ values by restricting air-sea gas exchange24,27. Cosmogenic isotope surface exposure dates obtained from erratic boulders

in the Hudson Mountains near Pine Island Glacier (Fig. 1) suggest that such an ice shelf had buttressed grounded ice upstream from PIB and that its thinning or collapse between 8.3 and 7.5 ka triggered rapid ice-stream thinning by >100 m (ref. 31).

Age constraints on cores PS75/160 and PS75/167 are based on previously published19,21 and newly calibrated AMS ^{14}C dates on calcareous microfossils (Extended Data Table 1). The recent chronology for core PS69/251, whose modern surface age has been confirmed by core-top AMS ^{14}C dating19, is constrained by a lead isotope (^{210}Pb) down-core profile (Extended Data Figs. 2-4, Extended Data Table 2). Core PS75/160, which spans the time period from ~9.2 to 1.2 kyr BP (Fig. 2a), was retrieved from a local depression in PIB at a water depth of just 337 m. The relatively shallow location of this core explains the abundant occurrence of calcareous microfossils, but another consequence is that the lowermost part of the core, older than ~8.2 kyr BP, is affected by iceberg or ice-shelf keel ploughing19 (Fig. 2). We overcome this issue by splicing the δ^{13}C data from core PS75/160 with those from nearby core PS75/167, which span 10.4 to 8.2 kyr BP (Fig. 2b; Extended Data Fig. 1). Core PS75/167 does not contain calcareous microfossils in sediments younger than ~8.2 kyr BP. In the following we refer to the spliced record as the “PIB record”.

The benthic Mg/Ca ratios in core PS75/160 imply higher bottom-water temperatures before 7.5 kyr BP, indicating that warm CDW flooded PIB during the early Holocene (11.7-7.5 kyr BP) and that this inflow was reduced during the middle (7.5-4.0 kyr BP) to late Holocene (4.0-0 kyr BP) (Fig. 3c; Extended Data Fig. 6). Intensified early Holocene CDW inflow is corroborated by both the benthic and the planktic foraminiferal δ^{13}C ratios of the PIB record which increase from relatively low values between ~10.4 and 9.0 kyr BP to higher values that are maintained from 7.0 kyr BP until at least 1.2 kyr BP (Figs. 2, 3a,b). The benthic δ^{13}C ratios recorded during the early Holocene match the $\delta^{13}C_{DIC}$ range of pure CDW. The planktic δ^{13}C ratios during this time interval reflect the lower range of $\delta^{13}C_{DIC}$ values typical for modern Antarctic Surface Water (AASW)32 which in the ASE usually forms a 200-300 m thick surface layer7,10. This observation suggests that the reduced δ^{13}C ratios of *N. pachyderma* sin., which calcifies within this AASW layer28, are caused by effective admixture of unmodified CDW into AASW.

Reduced ^{12}C export to the seabed in PIB caused by a decrease in plankton productivity can be ruled out as the reason for the benthic foraminifer δ^{13}C shift towards higher values at the end of the early Holocene because this would have resulted in lower planktic foraminifer δ^{13}C values, i.e. opposite to what is observed. In addition, the Ba/Ti ratios and foraminifer concentrations in core PS75/160 indicate that biological production probably increased rather than decreased after ~7.5 kyr BP (Fig. 2, Extended Data Figs. 5, 7). An onset or intensification of air-sea gas exchange between the atmosphere and surface waters in PIB at 7.5 kyr BP might have resulted from a reduction in ice-shelf coverage. The ice-shelf break-up would be consistent with the productivity increase after 7.5 kyr BP because phytoplankton production on the Antarctic continental margin is mainly controlled by the availability of light29. Such a scenario is in agreement with several early Holocene benthic δ^{13}C values in the PIB record that are even lower than the δ^{13}C value of pure CDW as well as a few planktic δ^{13}C values that are lower than the δ^{13}C value of AASW (Figs. 2, 3a,b). This observed ^{13}C-depletion could be explained by advection of nearly pure CDW combined

with reduced air-sea carbon exchange caused by ice-shelf cover of PIB during the early Holocene30,31.

The stable oxygen isotope ($\delta^{18}O$) data obtained from the benthic and planktic foraminifer shells in the PIB record do not reveal an early to middle Holocene shift such as the $\delta^{13}C$ data (Extended Data Fig. 5). The $\delta^{18}O$ composition of water masses on the Antarctic continental shelf is not simply a function of temperature but strongly influenced by salinity. As a result of meteoric and glacial meltwater supply along the coast cold surface water masses have low $\delta^{18}O$ values relative to deep water masses32, with CDW not only being warmer but also much saltier than AASW7,10. Enhanced CDW advection to the ice margin in PIB during the early Holocene would have caused strong melting under ice shelves and at the grounding line, so that the resulting input of glacial meltwaters with low $\delta^{18}O$ values may have suppressed the archiving of a high $\delta^{18}O$ signal characteristic for CDW in the foraminiferal carbonate.

Benthic foraminifera and environment

The benthic foraminifer assemblages in core PS75/160 show a distinct change at ~7.5 kyr BP, when an assemblage dominated by *Nonionella bradii* and *Globocassidulina* species (*G. subglobosa*, *G. biora*) is replaced by an assemblage dominated by various *Angulogerina* species, especially *A. angulosa* (Methods), and when both total foraminifer concentration and arenaceous benthic foraminifer abundance increase (Fig. 2a, Extended Data Fig. 7). While both *Globocassidulina* species and *Angulogerina* species have been found in modern33,34 and Holocene35–38 sub-ice shelf settings, an assemblage dominated by *Angulogerina* observed on the eastern Antarctic Peninsula shelf has been attributed to an ice-shelf edge setting33. Also *Nonionella* spp. has been reported from modern33,34 and Holocene35,38 sub-ice shelf sediments but its dominance in benthic foraminifer assemblages is frequently related to high biological productivity39. Given that neither the benthic $\delta^{13}C$ values nor the Ba/Ti ratios indicate higher productivity during the early Holocene (Figs. 2, 3a), we interpret the *Globocassidulina* and *Nonionella* dominated assemblage to indicate ice-shelf presence. Our interpretation is consistent with the dominance of *Nonionella* species and *Globocassidulina* species in benthic foraminifer assemblages of early to late Holocene sediments from the part of the eastern Antarctic Peninsula shelf which had been permanently ice-shelf covered from 11.5 kyr BP until A.D. 2002 (refs. 35, 40).

We suggest that PIB remained covered by an extensive ice shelf from at least ~9.2 until ~7.5 kyr BP. This conclusion agrees with the high proportion of a distinct non-encrusted shell morphotype of *N. pachyderma* sin. in the early Holocene sediments of core PS75/160 (Fig. 2a), which is indicative of specimens of a ‘neanic’ (i.e. adolescent) to adult life stage41 (Extended Data Fig. 8e-g). In contrast, the middle and late Holocene sediments in core PS75/160 are dominated by an encrusted shell morphotype that is typical for a terminal life stage41 (Extended Data Fig. 8a-d). We explain the dominance of the adolescent and adult shells by foraminifer reproduction in seasonal open water offshore from the ice shelf covering PIB, the subsequent advection of these foraminifera under the ice shelf by ocean currents, and their demise in this inhospitable environment for zooplankton, i.e. before they

could reach the terminal life stage. A contributing factor for the observed down-core change in the abundance of the two morphotypes of *N. pachyderma* sin. may be a deepening of the pycnocline. Under ice shelves the pycnocline lies deeper than in open water7,10 and is overlain by a cool mixed layer, in which non-encrusted morphotypes are concentrated41. Given the modern water depth of 337 m at site PS75/160 and taking into account the 30-10 m lower global sea level42 and the predicted ~50 m of seafloor depression in response to glacial loading of the PIB hinterland between 10 and 7.5 kyr BP43, the thickness of this early Holocene ice shelf cannot have exceeded ~410-430 m, which is comparable to the modern thicknesses of Thwaites Glacier Ice Shelf, Ronne Ice Shelf (West Antarctica) and Amery Ice Shelf (East Antarctica) near their calving fronts8,44.

Ice-shelf cover of PIB during the early Holocene would have contributed to the low benthic and planktic $\delta^{13}C$ values recorded during that time. However, bottom-water temperatures under ice shelves are lower than in seasonal open-marine settings10,44, whereas the benthic Mg/Ca data from PIB imply that these temperatures were higher in the proposed early Holocene sub-ice shelf environment than in the middle to late Holocene open-marine setting. Consequently, enhanced CDW supply onto the ASE shelf must have been the dominant factor influencing the early Holocene $\delta^{13}C$ record from PIB, even if ice-shelf cover contributed to low benthic $\delta^{13}C$ values. The most plausible scenario for explaining the changes in the foraminiferal carbon isotope composition and the bottom-water temperature around ~7.5 kyr BP is the reduction of CDW inflow. We conclude that compared to the present-day CDW advection onto the ASE shelf, which can be evaluated from the modern benthic and planktic $\delta^{13}C$ ratios, CDW inflow was stronger from 10.4 to about 8.0 kyr BP, while it was weaker from 7.5 to 1.2 kyr BP (Figs. 2, 3a,b).

Drivers of ice-sheet change

The early Holocene intensification of CDW heat supply can be attributed to a southerly position of the SHWW belt between 12.0 and 8.0 kyr BP45 (Fig. 3g,h). The northward shift of the westerlies from 8.0 to 6.0 kyr BP[45] is likely to have reduced CDW inflow as documented in the PIB record (Fig. 3). Thus, our findings expand on the conclusion from modern observational and modelling studies that the SHWW exert a major control on CDW advection onto the ASE shelf7,10,11,14. The role of buoyancy forcing9, however, remains unclear from our data. Early Holocene CDW advection may have been intensified along the entire Pacific margin of West Antarctica and thus may also explain the higher sea-surface temperatures observed on the western Antarctic Peninsula shelf during that time39,46 (Fig. 3e).

Grounded ice in PIB had retreated to within 110 km of its modern grounding line by 11.2 kyr BP19,21. Our conclusion of intensified CDW upwelling onto the ASE shelf from 10.4 to 7.5 kyr BP and probably since 12.0 kyr BP, when the SHWW already had a southerly position45, suggests that, in accordance with results from ice-sheet modeling15–17, ocean thermal forcing was the main driver of post-LGM WAIS retreat. In contrast, air temperatures in West Antarctica were still relatively low13 and post-glacial eustatic sea level had risen by not more than ~60 metres above its LGM low stand of -120 metres42,47 when PIB was already free of grounded ice, indicating that atmospheric and sea-level forcing played only a

subordinate role for post-LGM WAIS deglaciation (Fig. 3d,f). Sustained high CDW heat supply and accompanying oceanic melting might have destabilised any extensive ice shelf remaining in PIB until 7.5 kyr BP so that afterwards minor atmospheric warming in West Antarctica combined with continued global sea-level rise were sufficient to trigger its disintegration (Fig. 3d-f).

The modern benthic and planktic $\delta^{13}C$ ratios indicate that CDW inflow onto the ASE shelf must have increased at some time within the last millennium (Fig. 3a,b). The planktic $\delta^{13}C$ down-core record available from site PS69/251 on the outer ASE shelf, dating back to A.D. 1888±37 according to its ^{210}Pb chronology, reveals that this intensification took place between A.D. 1947±9 and A.D. 1963±9 (Fig. 4a). The increased CDW advection can be attributed to a strengthening and/or poleward shift of the SHWW, which is evident from proxy data in West Antarctic ice cores48,49 (Fig. 4b,c). Our finding is also consistent with recently published data from sub-ice shelf sediments showing that Pine Island Glacier started to retreat from a prominent sea-floor ridge in the mid-1940s, shortly after the a very large El Ninõ event from A.D. 1939 to 1942 (ref. 50). Together, these observations confirm the hypothesis that sea-surface temperature warming in the central tropical Pacific Ocean during the 1940s initiated the current period of CDW inflow onto the ASE shelf and the resulting mass loss in this sector of the WAIS12.

Importance

Our study extends the observational record of CDW inflow onto the ASE shelf further back in time through a period of significant ice-sheet change and it suggests early Holocene ice-shelf coverage in PIB. Most significantly, it provides the first empirical evidence for the dominant role of ocean forcing in driving past and recent WAIS deglaciation and the suggested control of CDW upwelling onto the ASE shelf by the SHWW. This information is crucial for validating assumptions in numerical models6,17,18 and will help to make model-based predictions of future global sea-level rise from Antarctic ice-sheet melting more robust.

Online Methods

Core material

Gravity cores PS75/160 and PS75/167 and giant box core PS75/215 were recovered on RV *Polarstern* expedition ANT-XXVI/3 in 2010 (ref. 51), while giant box core PS69/251 was retrieved during RV *Polarstern* expedition ANT-XXIII/4 in 2006 (ref. 52) (Extended Data Table 1). Sedimentological and/or chronological data for these cores have been previously published in Hillenbrand et al.19, Larter et al.21 and Smith et al.53.

Core processing, sedimentological analyses and chronologies

Methodologies of core processing and sedimentological analyses were reported by Hillenbrand et al.19, Larter et al.21 and Smith et al.53. Analytical techniques for AMS ^{14}C dating and calibrated AMS ^{14}C ages were also previously published19,21,53 but for this study we re-calibrated all conventional AMS ^{14}C dates from cores PS75/160 and PS75/167 (Extended Data Table 1). Because mixed calcareous (micro-)fossils, which are known to

show variable ^{14}C vital effects40, had been radiocarbon-dated from cores PS75/160 and PS75/167, we used a marine reservoir age with a relatively large error (R + ΔR = 1,100±200 years) for their calibration19. In contrast, Larter et al.21 and Smith et al.53 applied a uniform marine reservoir age with a much smaller error (R + ΔR = 1,300±70 years) to their calibration. Calibration was conducted using the CALIB 7.1 calibration programme54 using the MARINE13 (100%) calibration curve55.

All reported and calibrated AMS ^{14}C dates for core PS75/167 increase down-core or overlap within error but no ^{14}C dates could be obtained from above 230 cm depth (Fig. 2b; Extended Data Table 1). The ^{14}C dates for core PS75/160 show an age reversal below ~400 cm core depth (Fig. 2a; Extended Data Table 1). A thick unit of a distinct lithofacies (facies MC: deformed, sheared pebble-sized muddy to sandy soft sediment clasts randomly orientated in muddy matrix) occurs below this depth (Fig. 2a) suggesting that this lower part of core PS75/160 was affected by post-depositional turbation of the seafloor sediments by iceberg or ice-shelf keels19. Rather than ignoring the two trace metal (i.e. Mg/Ca) data and the benthic foraminifer assemblage data obtained from samples taken below this depth, we assigned for those samples ages by linear interpolation between maximum and minimum calibrated AMS ^{14}C dates of neighbouring age-depth fix points. This approach leaves some uncertainty in the absolute ages for the corresponding samples but an early Holocene age for the lower part of core PS75/160 is documented by the available AMS ^{14}C dates (Fig. 2a; Extended Data Table 1). We spliced the stable carbon isotope (δ^{13}C) records of cores PS75/160 and PS75/167 at 8.2 kyr BP (Extended Data Fig. 1) and display in panels **a** and **b** of Figure 3 exclusively δ^{13}C data from below 230 cm depth in core PS75/167 for the time interval >8.2 kyr BP and from above 380 cm depth in core PS75/160 for the time interval <8.2 kyr BP.

Radiocarbon dating of planktic foraminifera (*Neogloboquadrina pachyderma* sinistral) from undisturbed seafloor surface sediment retrieved in giant box core PS69/251 provided an uncorrected AMS ^{14}C age of 1,144±37 years19,53 and thus the youngest ^{14}C date obtained from modern surface sediments from the continental shelf in the Amundsen and Bellingshausen seas21 (Extended Data Table 1). As calcareous microfossil material was insufficient for AMS ^{14}C dating in samples taken from below the surface, lead-210 (^{210}Pb) dating and caesium-137 (^{137}Cs) dating were applied to core PS69/251 for establishing ages of down-core samples. The ^{210}Pb and ^{137}Cs activities were measured on 1 cm thick sediment slices by gamma-spectrometry using Canberra ultra-low-background Ge-detectors at the Gamma Dating Centre, Department of Geosciences and Natural Resource Management, University of Copenhagen. ^{210}Pb was measured from its gamma-peak at 46.5 keV, ^{226}Ra from the granddaughter ^{214}Pb (peaks at 295 and 352 keV) and ^{137}Cs from its peak at 661 keV. The core showed surface contents of unsupported ^{210}Pb of ~115 Bq kg^{-1} with a tendency for exponential decline with depth in the upper 6 cm (Extended Data Fig. 2a). Below ~6 cm core depth the ^{210}Pb activity was at the detection limit or lower. The calculated flux of unsupported ^{210}Pb is 100 Bq m^{-2} yr^{-1} which is in reasonable agreement with the expected flux from atmospheric deposition56. The content of ^{137}Cs was generally very low (Extended Data Fig. 2b). Constant Rate of Supply (CRS) modelling was applied on the ^{210}Pb profile using a modified method56 where the activity below 6 cm depth was

calculated on the basis of a regression (Extended Data Fig. 3). The ^{210}Pb dating results are given in Extended Data Table 2 and Extended Data Figure 4.

X-ray fluorescence scanning

Semi-quantitative uncalibrated major and trace element composition of cores PS75/160 and PS75/167 were analysed at the Alfred Wegener Institute, Bremerhaven, using an Avaatech XRF core scanner57. We applied XRF core scanning predominantly for the determination of the barium/titanium (Ba/Ti) peak-area ratio (hereafter referred to as the Ba/Ti ratio), which is a proxy for biogenic barium (Ba_{bio}). Ba_{bio} is considered to be the most reliable palaeoproductivity proxy in Antarctic continental margin sediments and Southern Ocean sediments south of the Antarctic Polar Front29,58–60. Following Weltje and Tjallingi61 we plotted the log-normalised [LN(Ba/Ti)] peak-area ratios in Figures 2 and Extended Data Figure 5. In order to assess down-core changes in the input of barium that is incorporated in the terrigenous heavy mineral barite we also calculated the log-normalised barium/zirconium (Ba/Zr) peak-area ratios [LN(Ba/Zr)], with Zr being a proxy for the terrigenous heavy mineral zircon (Extended Data Fig. 5).

Stable carbon and oxygen isotope analyses

Stable carbon ($\delta^{13}C$) and oxygen ($\delta^{18}O$) isotope analyses were performed on the planktic foraminifer species *Neogloboquadrina pachyderma* sinistral (12-24 shells; morphotype 1) and the epibenthic to shallow infaunal foraminifer *Angulogerina angulosa* (= *Trifarina angulosa)* (5-20 shells) (Extended Data Figs. 5, 7). The $\delta^{13}C$ and $\delta^{18}O$ isotopes were measured on 104 planktic and 112 benthic foraminifer samples from cores PS75/160 and PS75/167, one benthic foraminifer sample from site PS75/215 and seven planktic foraminifer samples from core PS69/251. The shells were picked from the wet sieved 63-2000 μm sediment size fraction and analysed at the Godwin Laboratory for Palaeoclimate Research at the Department of Earth Sciences, University of Cambridge (UK). Foraminifer shells were first crushed and soaked in a solution of 3 % H_2O_2 for 30 minutes, then acetone was added and the sample ultrasonicated for 10 seconds before the liquid was decanted. Samples were then dried at 50 °C overnight. Vials were sealed with septa and screw caps and analysed using a Micromass Multicarb sample preparation system attached to a VG SIRA Mass Spectrometer. Each run of 30 samples was accompanied by ten reference carbonates and two control samples. Results are reported with reference to the international standard Vienna Pee Dee Belemnite (VPDB), and analytical precision is better than ±0.06 ‰ for $\delta^{13}C$ and ±0.08 ‰ for $\delta^{18}O$. In this study, we only used the $\delta^{13}C$ data of *A. angulosa* and *N. pachyderma* sin. The $\delta^{13}C$ data of *A. angulosa* and *N. pachyderma* sin. were corrected for vital effects by adding +0.85 ‰ (cf. ref. 23) and +1.0 ‰ (refs. 27, 28), respectively.

Trace metal analyses

Ten samples from core PS75/160 contained sufficient calcareous benthic foraminifer shells of *A. angulosa* (200-300 μg) and ten samples from this core contained sufficient planktic foraminifer shells of *N. pachyderma* sin. (300-500 μg) for trace metal analyses. Samples were only taken from horizons with a lithofacies that does not indicate signs of reworking (i.e. no samples were taken from facies MC; Fig. 2a).

Europe PMC Funders Author Manuscripts

Cleaning of the shells followed the procedure described in Barker et al.62. Element ratios were determined by ICP-OES63 and ICP-MS64. Long-term instrumental precision of element ratio data, determined by replicate analyses of a standard solution containing magnesium/calcium (Mg/Ca) = 1.3 mmol mol^{-1}, was ±0.46 % r.s.d. Accuracy of Mg/Ca determinations was confirmed by inter-laboratory studies of foraminifer and carbonate reference materials65,66.

Iron/calcium (Fe/Ca) and manganese/calcium (Mn/Ca) were measured to monitor cleaning efficiency and diagenetic effects. The *N. pachyderma* sin. samples contained high Fe/Ca and Mn/Ca (up to 0.40 and 2.48 mmol mol^{-1}, respectively) with strong positive correlation between Mg/Ca, Fe/Ca (r^2 = 0.93) and Mn/Ca (r^2 = 0.94), reflecting diagenetic coating of the shells67 not removed by the cleaning procedure. Therefore, the Mg/Ca data on *N. pachyderma* sin. were not interpreted. The *A. angulosa* samples contained much lower Fe/Ca and Mn/Ca (maximum 0.14 and 0.64 mmol mol^{-1}, respectively) with no correlation observed between Mg/Ca and Fe/Ca (r^2 = 0.02) and a smaller (but still significant) correlation between Mg/Ca and Mn/Ca (r^2 = 0.56). In order to evaluate the impact of any diagenetic Mg contribution on the Mg/Ca data, we applied a correction to the measured Mg/Ca of *A. angulosa* (Fig. 3c, Extended Data Fig. 6a), assuming Mg/Mn of a diagenetic coating is 0.15±0.05 mol mol^{-1}, reflecting average composition of Mn nodules and ferromanganese crusts68,69, especially of those from the South Pacific and Pacific sector of the Southern Ocean70–72. The adjusted Mg/Ca ratios show the same (although less pronounced) down-core trend as the non-adjusted Mg/Ca data, with higher Mg/Ca ratios found before 7.5 kyr BP (Extended Data Fig. 6a,b). Also use of other Mg/Mn ratios for diagenetic coatings69 still indicates that the early to middle Holocene decrease in our Mg/Ca data is a robust feature (Extended Data Fig. 6b).

Boron/Calcium (B/Ca) was analysed on all. *A. angulosa* and *N. pachyderma* sin. samples aiming to exclude an influence of alkalinity on the Mg/Ca records73,74. Neither the benthic nor the planktic foraminiferal data show a correlation between Mg/Ca and B/Ca. However, B/Ca values measured on the *A. angulosa* shells were very low, in the range 7.1 to 13.0 μmol mol^{-1}, and probably influenced by the laboratory blanks. Consequently, the B/Ca data were not interpreted.

The Mg/Ca composition of calcareous foraminifer shells is frequently used as a quantitative proxy for seawater temperature20,75 but can also be controlled by the carbonate ion concentration ($[CO_3^{2-}]$) in the ambient seawater73,76. Consequently, higher Mg/Ca ratios as observed in core PS75/160 during the early Holocene (Fig. 3c, Extended Data Fig. 6) indicate an increase in either the temperatures and/or the $[CO_3^{2-}]$ of the deep-water mass flooding Pine Island Bay (PIB) during that time. The influence of the latter can be evaluated by measuring the B/Ca ratio of the foraminifer shells73,76,77, which, however, provided only inconclusive results for our samples from core PS75/160 (see above). The pre-industrial $[CO_3^{2-}]$ in Antarctic Surface Water (AASW) was 120 μmol kg^{-1} (ref. 28), whereas Circumpolar Deep Water (CDW) is characterised by a uniform, relatively low $[CO_3^{2-}]$ of 84±5 μmol kg^{-1} throughout the Southern Ocean, including its Pacific sector and the region south of the Antarctic Polar Front78. If the elevated benthic foraminiferal Mg/Ca ratios in PIB recorded during the early Holocene were caused by the presence of an AASW-like

water mass that comprised the entire water column, the corresponding benthic foraminiferal $\delta^{13}C$ ratios can be expected to resemble $\delta^{13}C_{DIC}$ values typical for AASW. In contrast, our early Holocene benthic foraminiferal $\delta^{13}C$ data from cores PS75/160 and PS75/167 are lower and typical for CDW (Figs. 2, 3b, Extended Data Fig. 5) and thus not consistent with a scenario that deep water present on the shelf of the Amundsen Sea Embayment (ASE) during that time was derived from AASW with the benthic Mg/Ca data reflecting its higher $[CO_3^{2-}]$.

Deep-water warming on the ASE shelf could have resulted either from intensified CDW upwelling or CDW warming. CDW warming would have resulted from a higher influx of North Atlantic Deep Water (NADW), which is the source water mass for CDW, into the Southern Ocean. NADW is injected into the clockwise flowing Antarctic Circumpolar Current in the Atlantic sector of the Southern Ocean, mixes with recirculated deep waters from the Indian and Pacific oceans, and, most importantly, acts as the “heat source” for CDW79. The $[CO_3^{2-}]$ of NADW is ~125 μmol kg^{-1} compared to only 84±5 μmol kg^{-1} in CDW78. Thus, intensified NADW influx into the Southern Ocean during the early Holocene, which is supported by marine sedimentary records from the Atlantic sector80, would have raised both the temperature and the $[CO_3^{2-}]$ in deep water flooding the ASE shelf, consistent with our Mg/Ca data from PIB. The $\delta^{13}C_{DIC}$ of NADW is higher than in CDW81. Consequently, increased NADW supply would have raised the $\delta^{13}C_{DIC}$ of CDW. This, however, is in conflict with the early Holocene benthic foraminiferal $\delta^{13}C$ data from our PIB cores, which are characterised by low values typical for CDW (Figs. 2, 3b; Extended Data Fig. 5). Therefore, the elevated benthic foraminiferal Mg/Ca ratios recorded in PIB during the early Holocene must reflect deep water warming caused by intensified CDW upwelling.

Analyses of benthic foraminifer assemblages

A total of 38 samples (1 cm thick sediment slices) were taken from core PS75/160 for benthic foraminifer analysis82. As with the trace metal samples, no samples were taken from the core section with lithofacies MC between 405 and 485 cm depth. The samples were washed through a 63 μm mesh-size sieve before the coarse residue was dry-sieved over 2 mm. All samples were screened in order to estimate the abundance of foraminifera. 27 samples with a relatively high content of foraminifera were selected for microscopic analysis and then dry-sieved over 125 μm and 250 μm. 23 of the 27 samples contained >300 benthic foraminifer shells in the >125 μm fraction. Samples with significantly more than 300 specimens and/or a large sample volume were split using a traditional hand-splitter until a suitable aliquot remained. Picked foraminifera were then identified under an optical microscope and by using Scanning Electron Microscope (SEM) images. Classification and identification were carried out in accordance with literature on recent Antarctic foraminifera (for full reference list, see Poole82).

Throughout core PS75/160, abundances of foraminifera are high, with total numbers ranging from 81 to 1,511 specimens per sample, and over 14,000 total specimens were identified from all samples82. The 27 samples yielded 84 benthic taxa but only one planktic species (*N. pachyderma* sin.). Between 0 and 341.5 cm core depth the abundance of foraminifera per

gram of dry sediment (foraminifera g^{-1}) is substantially greater than from 352.5 to 653.5 cm core depth, and there is a large range throughout the core (maximum: 306.19 foraminifera g^{-1} at 281.5 cm; minimum: 1.85 foraminifera g^{-1} at 631.5 cm) (Extended Data Fig. 7). Between 0 and 341.5 cm core depth, the average concentration of 102.58 foraminifera g^{-1} far exceeds the average concentration of only 20.81 foraminifera g^{-1} between 352.5 and 653.5 cm core depth.

Benthic calcareous species dominate the assemblages throughout the core while the abundance of arenaceous species accounts for a maximum of 30 % (depth: 141 cm) (Extended Data Fig. 7). Over two-thirds of samples comprise more than 85 % calcareous foraminifera82. However, arenaceous foraminifera are more abundant between 0 and 341.5 cm (mean: 15.2 %) than between 352.5 and 653.5 cm (mean: 7.0 %). *N. pachyderma* sin. is not particularly abundant, contributing a maximum of 5.5 % to the total assemblage at 281.5 cm, though it is present in all samples. Preservation of benthic and planktic foraminifer shells was good to moderate throughout the core.

The upper section of core PS75/160 from 0 to 341.5 cm depth typically contains high abundances and percentages of the calcareous benthic species *Angulogerina angulosa*, *A.* sp. 1, *Uvigerina* sp. 1, *Globocassidulina subglobosa*, and *G. biora* (Extended Data Fig. 7). Relatively abundant accessory species include *Astrononion echolsi*, *Alabaminella weddellensis* and the arenaceous species *Miliammina arenacea*, *Portatrochammina* sp. 1 and *Labrospira jeffreysii*. We follow previous researchers on benthic foraminifera from the Antarctic continental margin and summarize under '*A. angulosa*' the species *A. angulosa, A. earlandi*, *Trifarina angulosa* and *T. earlandi*36,83–85, which are morphospecies rather than separate biological species (cf. refs. 86–88). Moreover, molecular genetic data have shown that *Angulogerina*/*Trifarina* is closely related to *Uvigerina peregrina*88,89, with which it also shares the epifaunal to shallow infaunal habitat23,83,90.

A major faunal change was observed between 341.5 and 352.5 cm core depth. The section below this depth is characterised by low abundances of *A. angulosa* and *A. pauperata*. This lower core section is dominated by *Nonionella bradii*, *N. iridea*, *G. subglobosa*, and *G. biora* (Extended Data Fig. 7). The subsidiary species include *Ehrenbergina glabra*, *Fursenkoina fusiformis* (calcareous), and *Portatrochammina* sp. 1 (arenaceous). The planktic foraminifera in this lower core section are dominated by *N. pachyderma* sin. type 2, while *N. pachyderma* sin. type 1 dominates the upper section (Extended Data Figs. 7, 8). Principal Component Analysis (PCA), Correspondence Analysis (CA) and Cluster Analysis demonstrate that the pronounced change between the two dominant benthic foraminifer assemblages between 341.5 and 352.5 cm core depth is statistically robust82.

Data availability statement

The stable isotope ($\delta^{13}C$, $\delta^{18}O$), trace metal (Mg/Ca, Mn/Ca), XRF scanner (Ba/Ti, Ba/Zr), benthic foraminifer assemblage and chronological (AMS ^{14}C, ^{210}Pb) data reported in this paper are available in the PANGAEA database under doi:10.1594/PANGAEA.XXX [*number to be assigned after final acceptance*] and from the corresponding author by request. Metadata, detailed core descriptions, X-radiographs, physical properties and grain size data of the cores are available under doi.pangaea.de/10.1594/PANGAEA.751493.

Europe PMC Funders Author Manuscripts

Extended Data

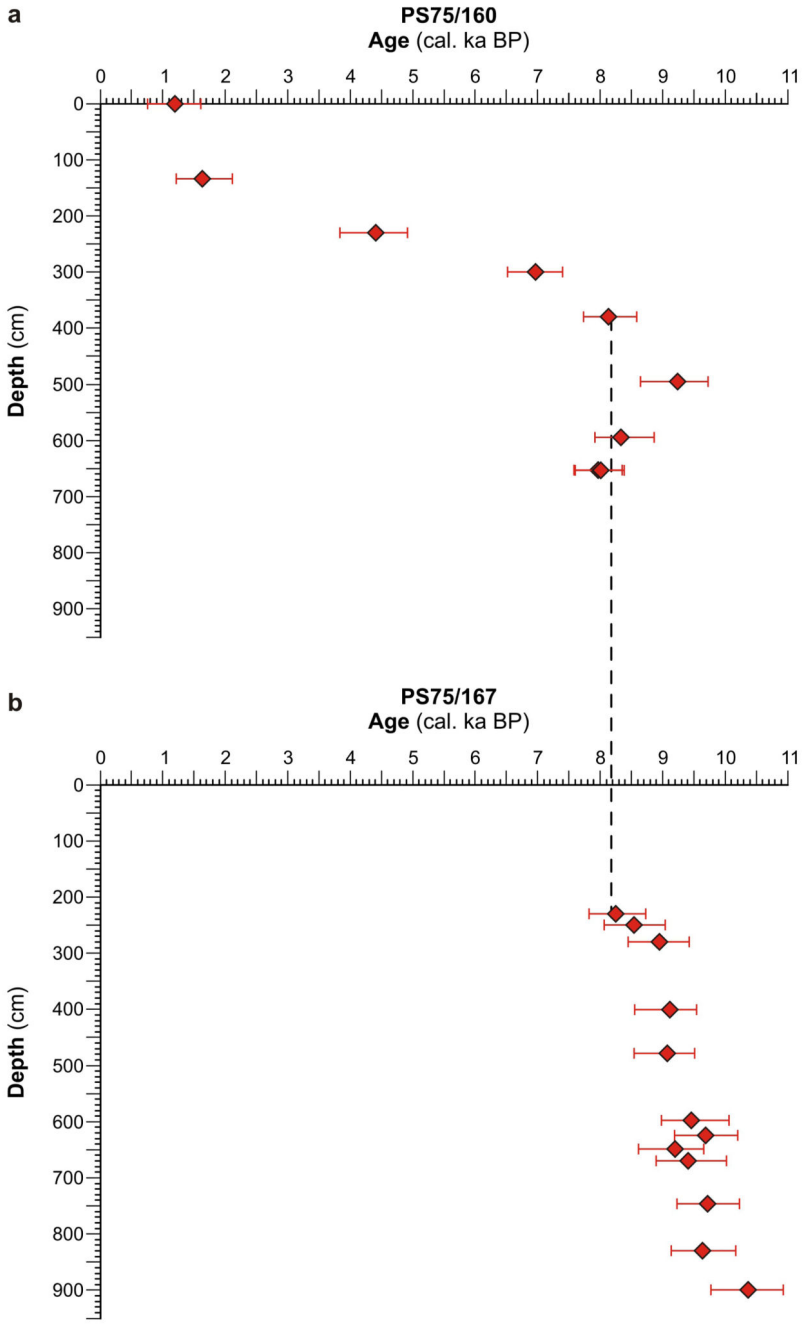

Extended Data Figure 1. Radiocarbon chronologies for Holocene sediments from Pine Island Bay.

The age-depth plots for cores PS75/160 (**a**) and PS75/167 (**b**) are based on AMS ^{14}C dates obtained from calcareous microfossils (Extended Data Table 1). The red diamonds mark the calibrated median AMS ^{14}C ages, with the error bars indicating the maximum and minimum ages. The vertical dashed line marks the overlapping age of 8.2 kyr BP, corresponding to 380

cm depth in core PS75/160 and 230 cm depth in core PS75/167, where the benthic and planktic $\delta^{13}C$ records of the two records were spliced (Fig. 3a, 3b).

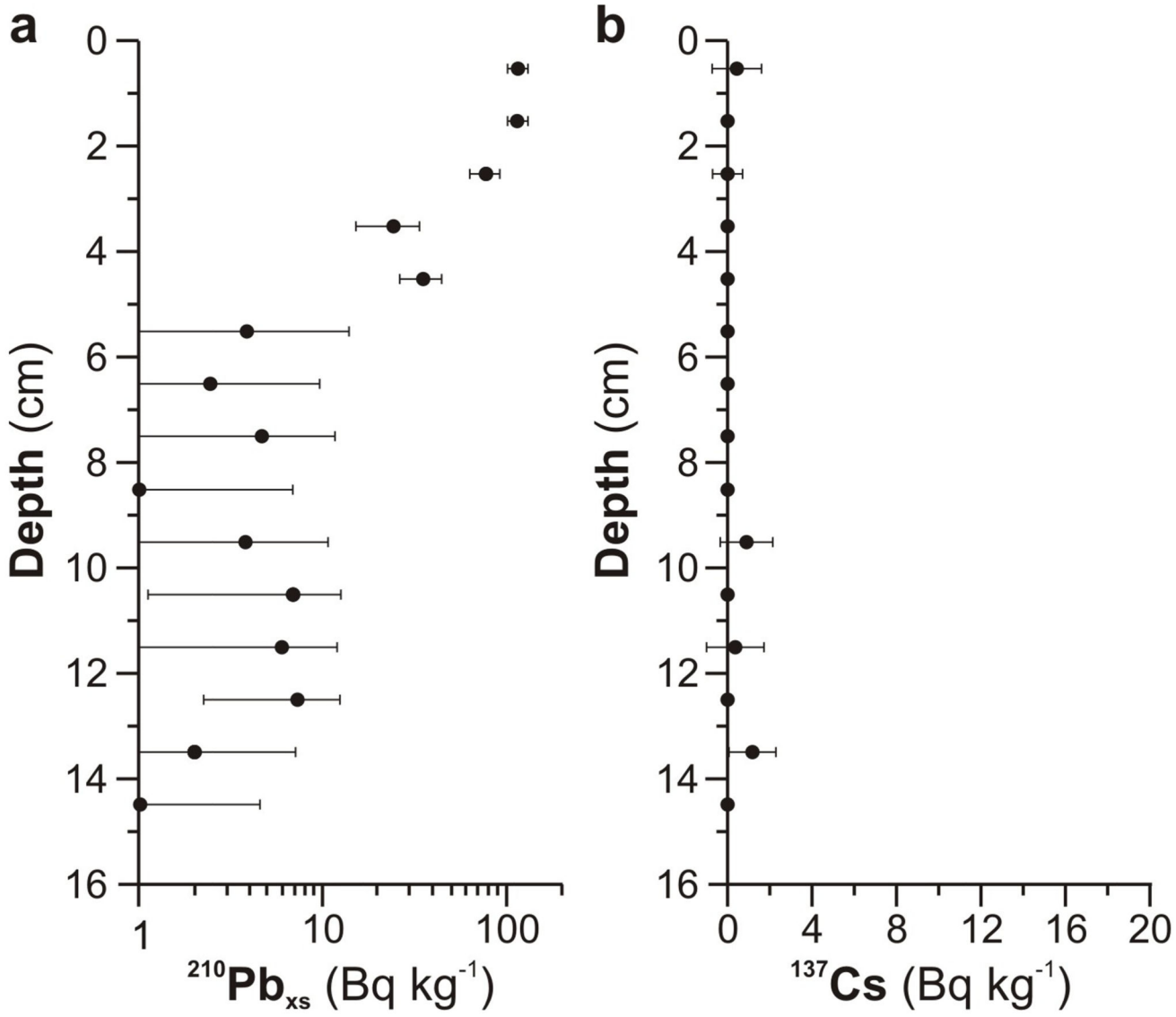

Extended Data Figure 2. Down-core concentrations of radiogenic lead and caesium isotope concentrations in sediments from the outer Amundsen Sea shelf.

The concentration of unsupported ^{210}Pb ($^{210}Pb_{xs}$) for sediments from giant box core PS69/251 is displayed on a logarithmic scale (**a**), while the concentration of ^{137}Cs is displayed on a linear scale (**b**). Error bars denote 1 s.d. of the ^{210}Pb and ^{137}Cs concentrations. The $^{210}Pb_{xs}$ concentration is ~115 Bq kg^{-1} at the sediment surface and declines exponentially with core depth in the upper 6 cm. The ^{210}Pb activity is at the detection limit or lower below 6 cm depth. The calculated $^{210}Pb_{xs}$ flux is 100 Bq m^{-2} yr^{-1}, which is in reasonable agreement with the expected flux from atmospheric deposition[56]. The ^{137}Cs activity is at or below the detection limit throughout the core.

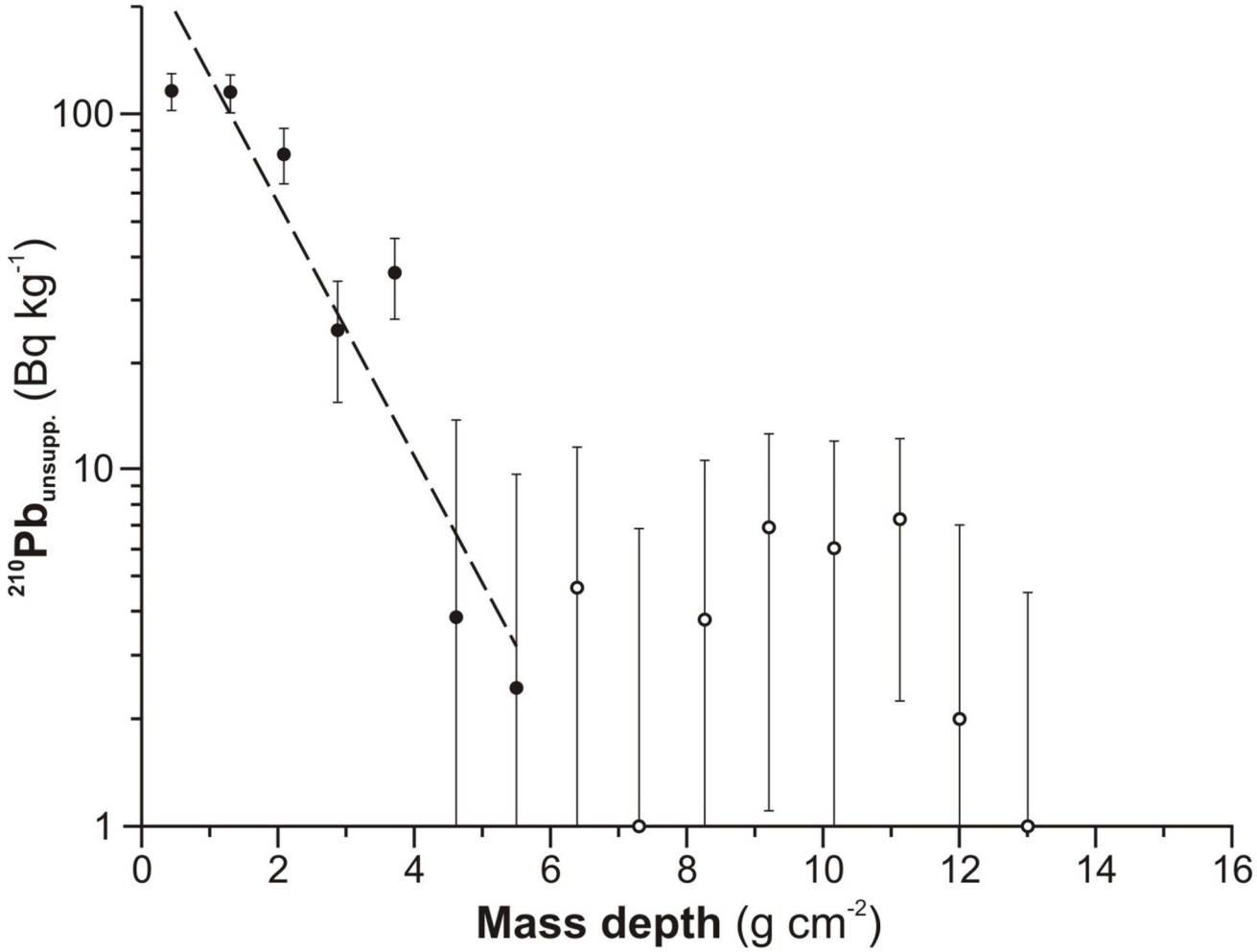

Extended Data Figure 3. Constant rate of supply (CRS) modelling of the down-core $^{210}Pb_{xs}$ profile on the outer Amundsen Sea shelf.

The CRS modelling was conducted on the sediments from core PS69/251 using a modified method56. The dashed line marks the regression used to calculate the ^{210}Pb concentration below 6 cm core depth. Open circles highlight samples with $^{210}Pb_{xs}$ concentrations at or below the detection limit. Error bars denote 1 s.d. of the $^{210}Pb_{xs}$ concentrations.

Europe PMC Funders Author Manuscripts

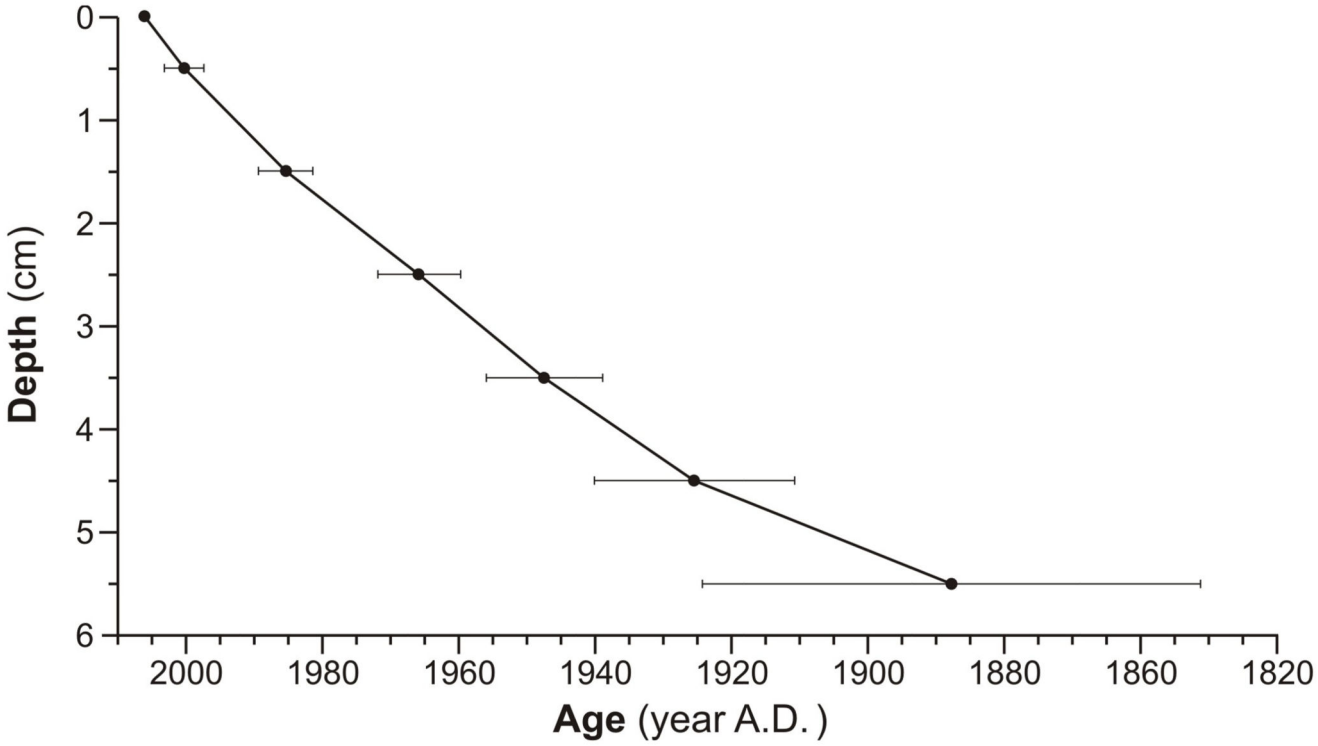

Extended Data Figure 4. Age-depth relationship for sediments from the outer Amundsen Sea shelf.

The age model for the sediments from core PS69/251 is based on CRS modelling of the down-core $^{210}Pb_{xs}$ profile in the uppermost part of the core. Error bars denote 1 s.d. of the calculated ages.

Europe PMC Funders Author Manuscripts

Europe PMC Funders Author Manuscripts

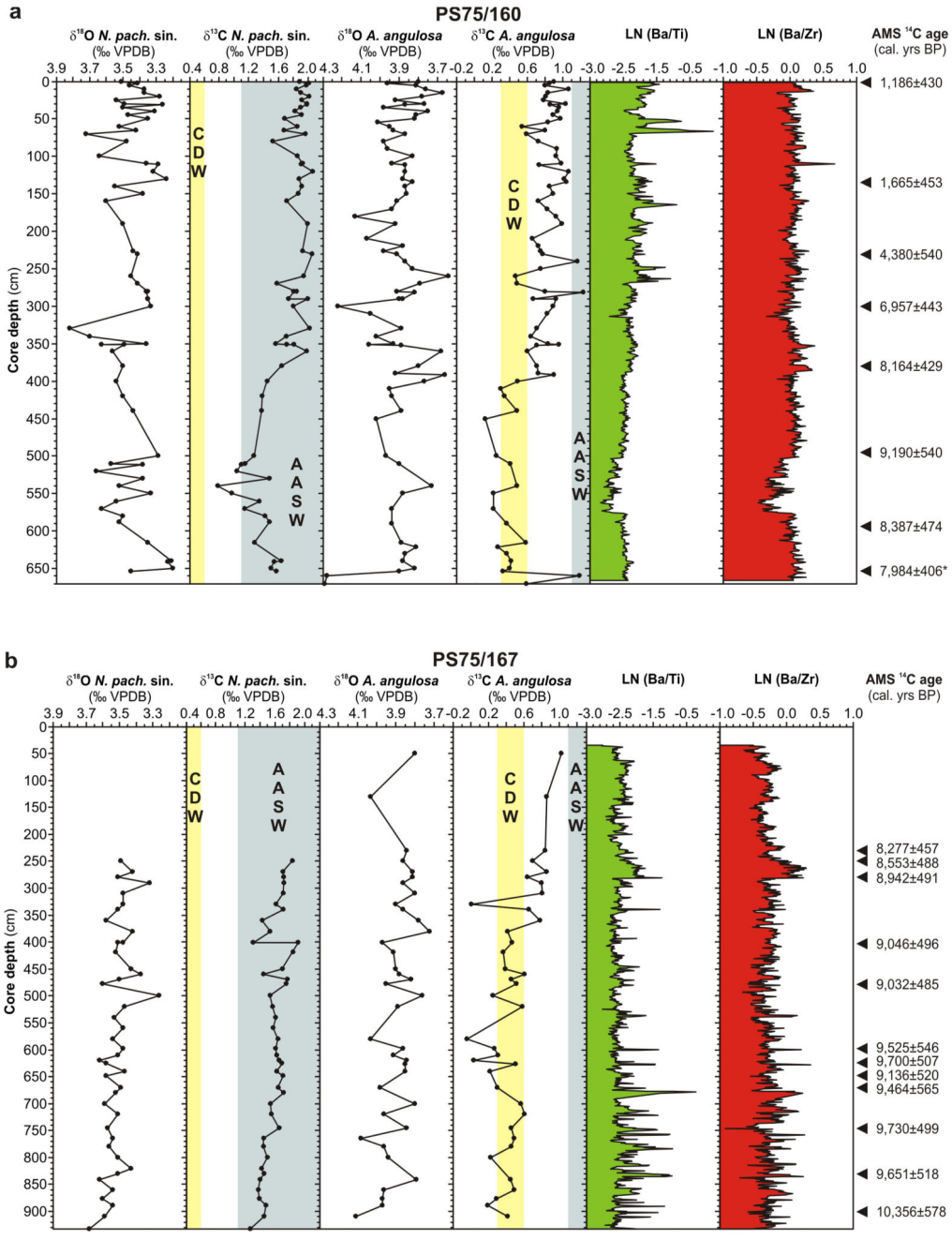

Extended Data Figure 5. Geochemical and chronological data of Holocene sediments from Pine Island Bay.

Down-core profiles of planktic (*N. pachyderma* sin.) and benthic (*A. angulosa*) $\delta^{18}O$ and $\delta^{13}C$ ratios, log-normalised Ba/Ti [LN(Ba/Ti)] and Ba/Zr [LN(Ba/Zr] peak area ratios61 and radiocarbon dates are shown for cores PS75/160 (**a**) and PS75/167 (**b**). AMS ^{14}C dates were obtained from various calcareous microfossils19,21,53 (Extended Data Table 1) and are displayed as mean calibrated ages with 2 s.d. error. The asterisk at the lowermost date from core PS75/160 indicates average of replicate dates from the same sample horizon. The

ranges of $\delta^{13}C$ values typical for AASW and CDW are indicated by the blue-green and yellow shaded areas, respectively. Seawater $\delta^{18}O$ composition reported for the ASE is about -0.7 ‰ to -0.5 ‰ with reference to the international Vienna Standard Mean Ocean Water (VSMOW) standard in AASW and -0.3 ‰ to -0.1 ‰ VSMOW in CDW91, yielding an offset of about -0.4 ‰ VSMOW between surface and deep waters. The average offset between the planktic and benthic $\delta^{18}O$ records of cores PS75/160 and PS75/167 is -0.45 ‰ VPDB and -0.38 ‰ VPDB, respectively, which is consistent with the reported surface to deep water $\delta^{18}O$ gradient (N.B.: relation between SMOW scale and VPDB scale is linear92). While prominent peaks in LN(Ba/Ti) below ~220 cm depth in core PS75/167 are significantly higher than the background LN(Ba/Ti) values, the LN(Ba/Zr) peaks are not significantly higher in this core section. This relation suggests that the LN(Ba/Ti) and Ba/Ti peaks are caused by barium input through increased supply of terrigenous heavy minerals (including barite and zircon), which is confirmed by the down-core increase of terrigenous sand layers below ~220 cm core depth (see Fig. 2 in ref. 19).

Europe PMC Funders Author Manuscripts

Europe PMC Funders Author Manuscripts

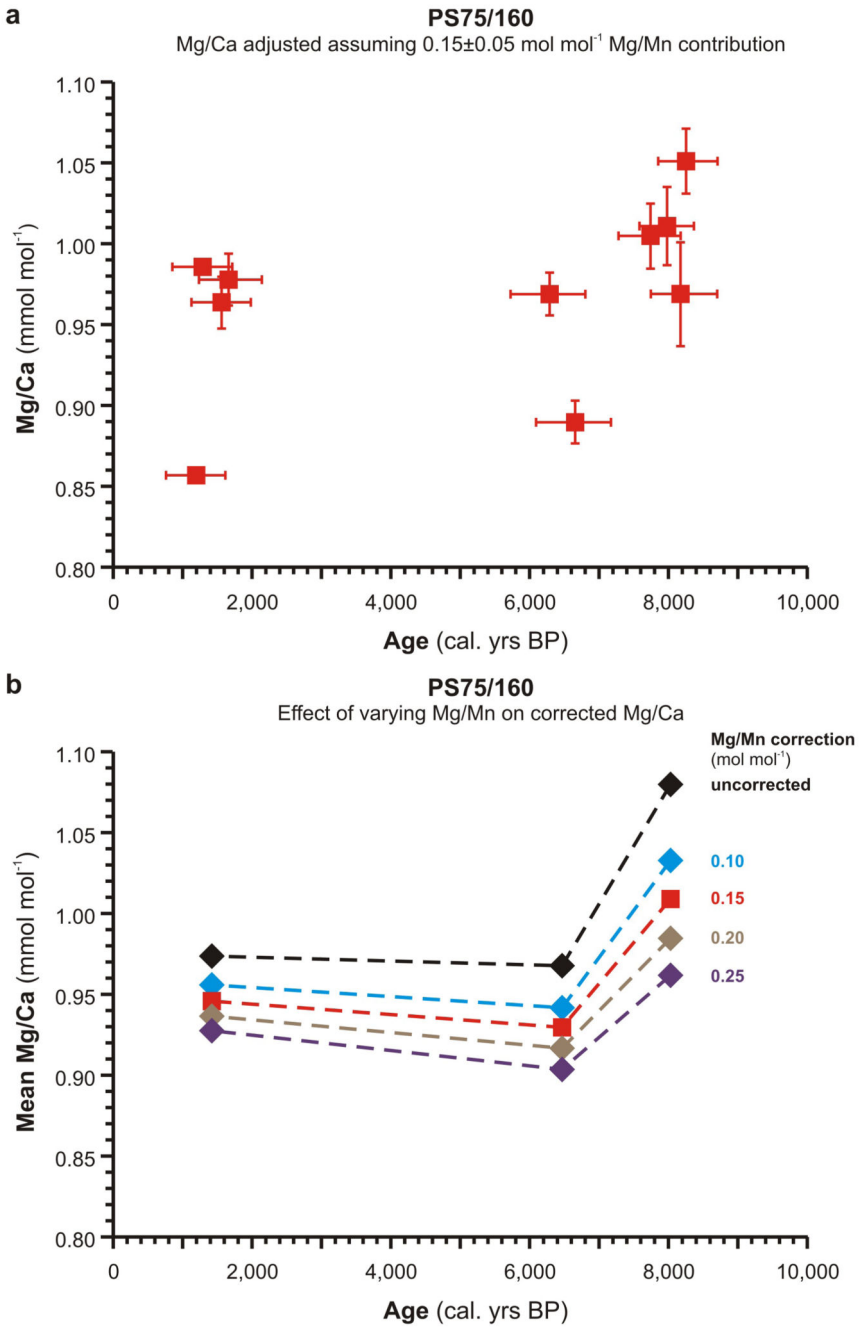

Extended Data Figure 6. Magnesium/calcium ratios of benthic foraminifer shells in Pine Island Bay.

The magnesium/calcium (Mg/Ca) ratios, which were measured on shells of the benthic foraminifer species *A. angulosa* from core PS75/160, are shown with an adjustment for a potential diagenetic Mg contribution by assuming a magnesium/manganese (Mg/Mn) ratio of 0.15±0.05 mol mol^{-1} in the diagenetic coating (**a**), and with an adjustment for a potential diagenetic Mg contribution by assuming a range of Mg/Mn ratios in the diagenetic coating (**b**). The Mg/Ca ratios in **b** are displayed as averages of samples taken from the time

intervals 10.0-7.5 kyr BP (4 samples), 7.5-4.0 kyr BP (2 samples) and 4.0-0 kyr BP (4 samples), both without adjustment and with adjustment for potential diagenetic Mg contributions assuming Mg/Mn ratios in diagenetic coatings of 0.10, 0.15, 0.20 and 0.25 mol mol^{-1} (references 68–72). Error bars in **a** highlight the uncertainty of ±0.05 mol mol^{-1} for the Mg/Mn composition of the coating and the 2 s.d. range of the ages of the Mg/Ca samples, which were calculated from the calibrated AMS ^{14}C dates obtained from neighbouring sample horizons (Extended Data Table 1).

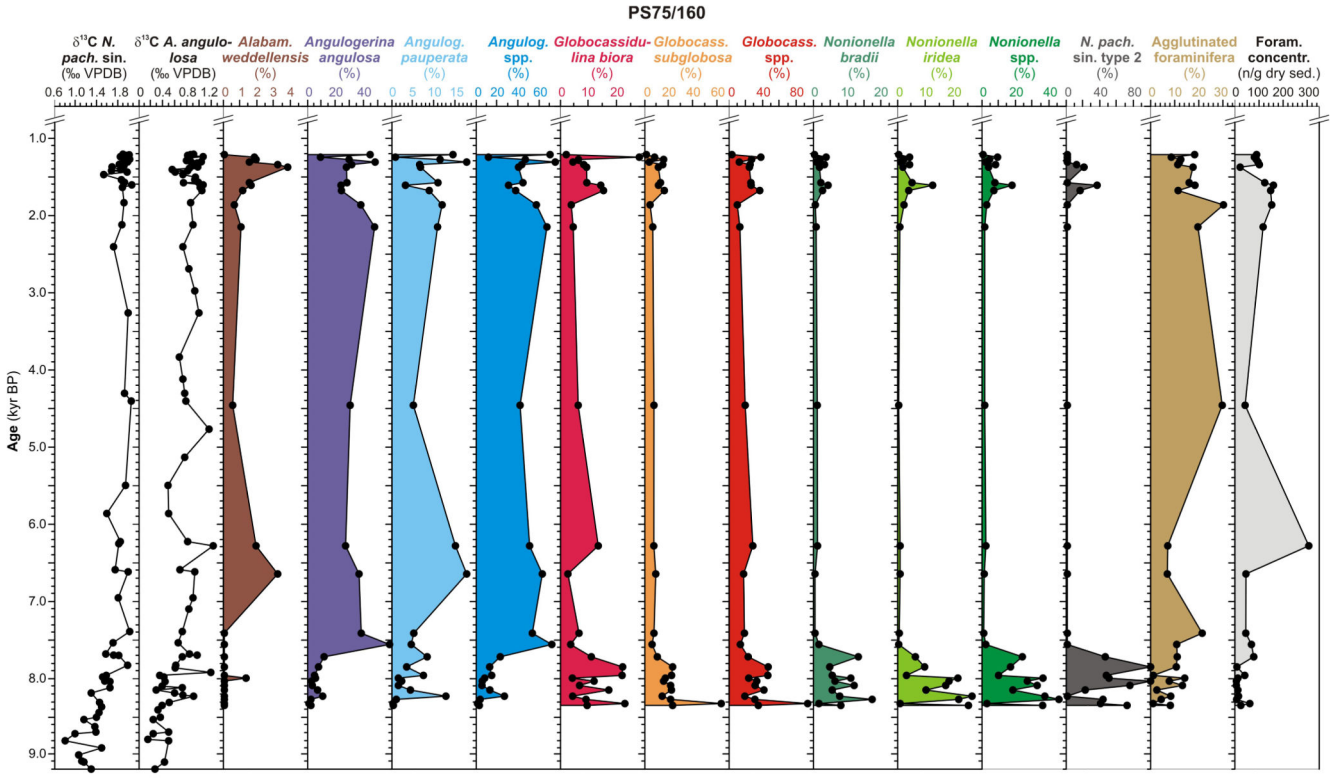

Extended Data Figure 7. Holocene changes in foraminifer assemblages from Pine Island Bay.

Benthic foraminifer assemblages (only the most abundant and selected benthic taxa are displayed), abundance of *N. pachyderma* sin. type 2 (in relation to all planktic foraminifera), abundance of arenaceous benthic foraminifera (in relation to all benthic foraminifera) and total foraminifer concentration (individuals per gram dry sediment) were analysed on core PS75/160. The $\delta^{13}C$ composition of planktic and benthic foraminifer shells is also shown. Note major shift in foraminifer abundances and assemblages centred at 7.5 kyr BP. Benthic foraminifer taxa: *Alabaminella weddellensis*, *Angulogerina angulosa*, *Angulogerina pauperata*, *Angulogerina* spp. (= sum of all *Angulogerina* species), *Globocassidulina biora*, *Globocassidulina subglobosa*, *Globocassidulina* spp. (= sum of all *Globocassidulina* species), *Nonionella bradii*, *Nonionella iridea*, *Nonionella* spp. (= sum of all *Nonionella* species).

Europe PMC Funders Author Manuscripts

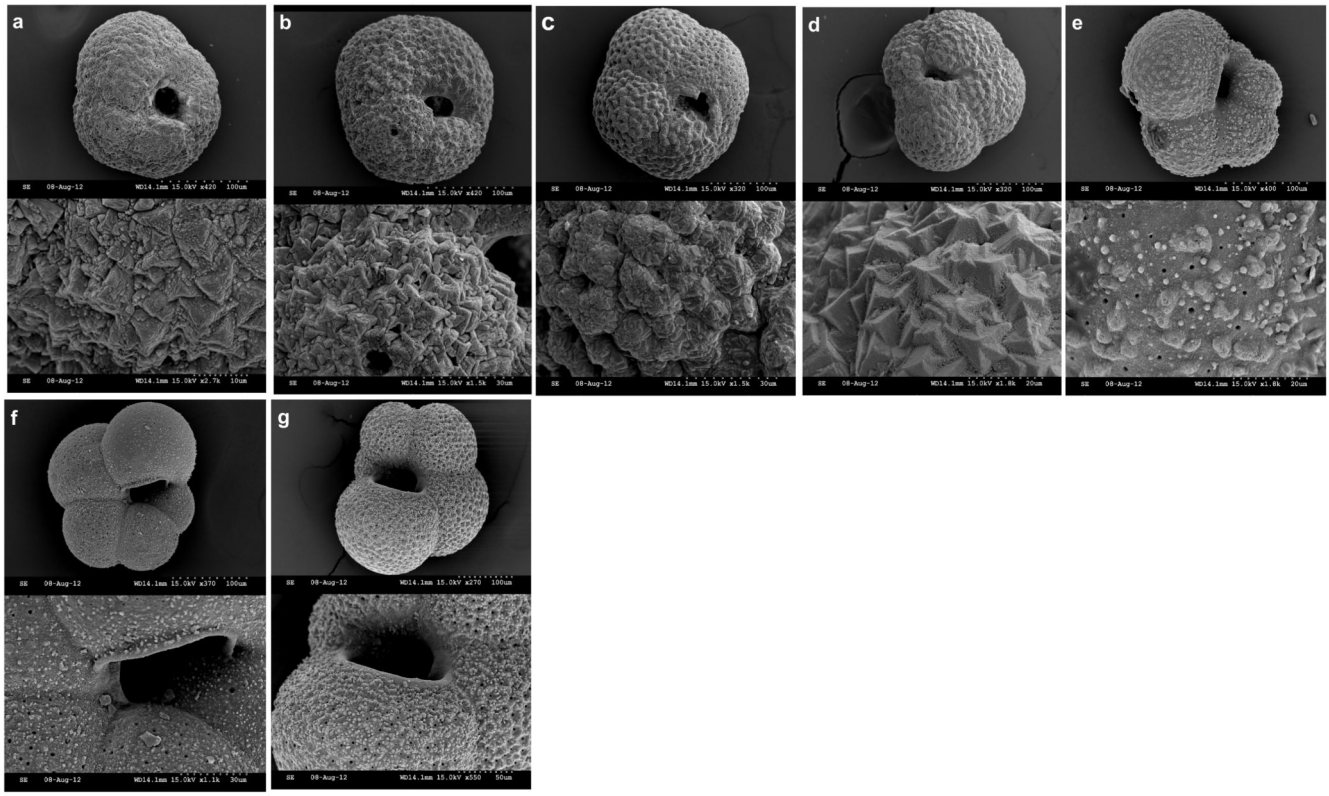

Extended Data Figure 8. Scanning Electron Microscope (SEM) images of planktic foraminifer shells in Holocene sediments from Pine Island Bay.

Whole shells and detailed shell surfaces of *Neogloboquadrina pachyderma* sinistral morphotypes 1 and 2 from core PS75/160 are shown. Morphotype 1 (**a-d**) is encrusted with gametogenic calcite and dominates the upper section of the core, while thin-walled and non-encrusted morphotype 2 (**e-g**) dominates the lower section of core PS75/160. A scale bar (white dots) is shown in the lower right corner of each photo, and the unit of its length (number) is given in μm. Note the indistinct chambers and gametogenic calcite secreted around the whole shell in morphotype 1, while the individual chambers and porous shells of morphotype 2 are clearly visible, thereby showing beginning encrustation (white calcite around pores) (cf. refs. 41, 93–95). Morphotype 1 usually dominates the lower part of the water column in Antarctic and Arctic waters and is preserved in marine sediments, whereas morphotype 2 is abundant in the upper part of the water column and not preserved in the sediments41,93–95. Encrusted morphotype 1 is typical for the terminal life stage of *N. pachyderma* sin., while non-encrusted morphotype 2 is typical for its neanic (i.e. adolescent) to adult stage41,93–96. In analogy with the SEM-defined progressive dissolution steps distinguished by Henrich97, the shells in images **a** and **b** are affected by intermediate dissolution, the shell in image **c** is affected by initial to intermediate dissolution, the shell in image **d** is affected by initial dissolution and the shells in images **e-g** are well preserved.

Europe PMC Funders Author Manuscripts

Extended Data Table 1

Locations, conventional and calibrated AMS ^{14}C dates on calcareous microfossils from the investigated sediment cores.

Coring devices: GBC: giant box core, GC: gravity core. Sample depths are given in centimetres below seafloor (cmbsf; top of CC: sample was taken from top of core catcher, corresponding to 652 cmbsf). All ^{14}C-dates were corrected using an offset (ΔR) of 700±200 years from the global marine reservoir effect (R) of 400 years. The corrected ^{14}C-dates were calibrated with the CALIB Radiocarbon Calibration Program version 7.1html54 (http://calib.qub.ac.uk/calib/) using the MARINE13 calibration dataset55. Uncorrected dates (= ^{14}C age) are given in ^{14}C years before present (BP) with their errors given as 1 s.d. range. Calibrated dates are given as maximum and minimum ages (2 s.d. range) as well as median and mean ages in calibrated years BP. Dated calcareous microfossils: bF: benthic foraminifera, Bp: brachiopods, Bz: bryozoans, E: echinoid spines, F: mixed benthic and planktonic foraminifera, O: ostracods, P: pteropods, pF: planktonic foraminifera, S: unspecified calcareous shell fragments.

Station and core ID	Latitude (°S)	Longitude (°W)	Water depth (m)	Recovery (m)	Sample depth (cmbsf)	Laboratory code	Dated material	^{14}C age ±1 s.d. (yr BP)	Max. age (yr BP)	Min. age (yr BP)	Med. age (yr BP)	Mean age (yr BP)
PS2544-1 GBC	71.796	105.191	546	0.21	surface	N/A	N/A	N/A	N/A	N/A	N/A	N/A
PS69/251-1 GBC	72.069	104.483	573	0.38	surface	SUERC-18942	pF	1144±37	N/A	N/A	[0]	[0]
PS75/215-1 GBC	74.592	104.042	556	0.62	surface	Beta-315966	Bz	1190±30	N/A	N/A	[0]	[0]
PS75/1 60-1 GC	74.564	102.624	337	6.68	0.5	Beta-284601	bF, S, O	2340±40	1615	756	1190	1186
					133.5	Beta-284602	S	2750±40	2118	1212	1634	1665
					230	Beta-284604	bF, S, O	4990±40	4919	3840	4405	4380
					300	Beta-284681	bF, S	7180±40	7400	6514	6967	6957
					380	Beta-284606	bF, S	8410±40	8592	7735	8137	8164
					490+500	Beta-284607	bF, P, S, O	9320±40	9729	8650	9243	9190
					588+600	Beta-284608	bF, S, O, Bp	8560±40	8861	7913	8331	8387
					652	Beta-284610	S	8200±40	8358	7578	7966	7968
					top of CC	Beta-284600	Bp, S, bF	8240±40	8390	7603	8006	7997
PS75/1 67-1 GC	74.623	105.802	526	9.34	230	Beta-300838	F	8490±40	8734	7820	8254	8277
					250	Beta-300839	F, S	8740±40	9040	8065	8547	8553
					280	Beta-284682	F	9080±50	9432	8451	8949	8942
					401	Beta-284683	F, S, O	9210±50	9541	8550	9113	9046
					478	Beta-300837	F, O, E	9180±40	9516	8547	9077	9032
					598	Beta-300840	F	9490±40	10070	8979	9459	9525

Europe PMC Funders Author Manuscripts

Station and core ID	Latitude (°S)	Longitude (°W)	Water depth (m)	Recovery (m)	Sample depth (cmbsf)	Laboratory code	Dated material	^{14}C age ±1 s.d. (yr BP)	Max. age (yr BP)	Min. age (yr BP)	Med. age (yr BP)	Mean age (yr BP)
					625.5	Beta-284684	F	9660±50	10206	9193	9690	9700
					649	Beta-300841	F	9280±40	9656	8616	9196	9136
					670	Beta-284685	F	9450±50	10029	8899	9405	9464
					746	Beta-284686	F, S	9690±50	10228	9231	9726	9730
					830	Beta-300842	F	9620±50	10169	9133	9640	9651
					900.5	Beta-284687	F, S	10210±60	10934	9778	10372	10356

Europe PMC Funders Author Manuscripts

Extended Data Table 2

Chronology of the upper 6 cm of core PS69/251 based on constant rate of supply modelling of the unsupported lead-210 concentration.

Errors for ages and mass accumulation rates are given as 1 s.d.

Depth (cm)	Age (yrs)	Age error (yrs)	Date (yrs A.D.)	Mass accumulation rate (kg m^{-2} yr^{-1})	Mass accumulation rate error (kg m^{-2} yr^{-1})
0			2006		
0-1	6	3	2000	0.78	0.10
1-2	21	4	1985	0.57	0.10
2-3	40	6	1966	0.41	0.10
3-4	59	9	1947	0.42	0.16
4-5	81	15	1925	0.38	0.19
5-6	118	37	1888	0.24	0.28

Acknowledgements

This study is part of the Polar Science for Planet Earth Programme of the British Antarctic Survey and the PACES II (Polar Regions and Coasts in the changing Earth System) programme of the Alfred-Wegener-Institut. It was funded by the Natural Environment Research Council (NERC), NERC grant NE/M013081/1 and the Helmholtz Association. This work was also funded (in part) by The European Research Council (ERC grant 2010-NEWLOG ADG-267931 HE). We thank the captain, crew, shipboard scientists and support staff participating in RV *Polarstern* expeditions ANT-XXIII/4 and ANT-XXVI/3, and are grateful to R. Downey, T. Williams, V. Peck, H. Blagbrough, R. Fröhlking and S. Wiebe for their assistance. Furthermore, we thank D. Hodgson, D. Vaughan and P. Dutrieux for discussions, S. Schmidtko for providing data and three anonymous referees for their thoughtful comments which helped to improve the paper.

References

1. Sutterley TC, et al. Mass loss of the Amundsen Sea Embayment of West Antarctica from four independent techniques. Geophys Res Lett. 2014; 41:8421–8428.
2. Mouginot J, Rignot E, Scheuch B. Sustained increase in ice discharge from the Amundsen Sea Embayment, West Antarctica, from 1973 to 2013. Geophys Res Lett. 2014; 41:1576–1584.
3. Rignot E, Mouginot J, Morlighem M, Seroussi H, Scheuch B. Widespread, rapid grounding line retreat of Pine Island, Thwaites, Smith, and Kohler glaciers, West Antarctica, from 1992 to 2011. Geophys Res Lett. 2014; 41:3502–3509.
4. Joughin I, Smith B, Medley B. Marine ice sheet collapse potentially under way for the Thwaites Glacier basin, West Antarctica. Science. 2014; 344:735–738. [PubMed: 24821948]
5. Favier L, et al. Retreat of Pine Island Glacier controlled by marine ice-sheet instability. Nature Climate Change. 2014; 4:117–121.
6. DeConto RM, Pollard D. Contribution of Antarctica to past and future sea-level rise. Nature. 2016; 531:591–597. [PubMed: 27029274]
7. Jacobs SS, Jenkins A, Giulivi CF, Dutrieux P. Stronger ocean circulation and increased melting under Pine Island Glacier ice shelf. Nature Geosci. 2011; 4:519–523.
8. Paolo FS, Fricker HA, Padman L. Volume loss from Antarctic ice shelves is accelerating. Science. 2015; 348:327–331. [PubMed: 25814064]
9. Wåhlin AK, et al. Variability of Warm Deep Water inflow in a submarine trough on the Amundsen Sea shelf. J Phys Oceanography. 2013; 43:2054–2070.
10. Dutrieux P, et al. Strong sensitivity of Pine Island Ice-Shelf melting to climatic variability. Science. 2014; 343:174–178. [PubMed: 24385606]
11. Thoma M, Jenkins A, Holland D, Jacobs S. Modelling Circumpolar Deep Water intrusions on the Amundsen Sea continental shelf, Antarctica. Geophys Res Lett. 2008; 35:L18602.
12. Steig EJ, Ding Q, Battisti DS, Jenkins A. Tropical forcing of Circumpolar Deep Water inflow and outlet glacier thinning in the Amundsen Sea Embayment, West Antarctica. Annals Glaciol. 2012; 53:19–28.
13. WAIS Divide Project Members. Onset of deglacial warming in West Antarctica driven by local orbital forcing. Nature. 2013; 500:440–444. [PubMed: 23945585]
14. Schmidtko S, Heywood KJ, Thompson AF, Aoki S. Multidecadal warming of Antarctic waters. Science. 2014; 346:1227–1231. [PubMed: 25477461]
15. Pollard D, DeConto RM. Modelling West Antarctic ice sheet growth and collapse through the past five million years. Nature. 2009; 458:329–333. [PubMed: 19295608]
16. Golledge NR, et al. Antarctic contribution to meltwater pulse 1A from reduced Southern Ocean overturning. Nature Communications. 2014; 5:5107.doi: 10.1038/ncomms6107
17. Pollard D, Chang W, Haran M, Applegate P, DeConto R. Large ensemble modeling of the last deglacial retreat of the West Antarctic Ice Sheet: comparison of simple and advanced statistical techniques. Geosci Model Dev. 2016; 9:1697–1723.
18. Golledge NR, et al. The multi-millennial Antarctic commitment to future sea-level rise. Nature. 2015; 526:421–425. [PubMed: 26469052]
19. Hillenbrand C-D, et al. Grounding-line retreat of the West Antarctic Ice Sheet from inner Pine Island Bay. Geology. 2013; 41:35–38.

20. Katz ME, et al. Traditional and emerging geochemical proxies in foraminifera. J Foram Res. 2010; 40:165–192.
21. Larter RD, et al. Reconstruction of changes in the Amundsen Sea and Bellingshausen Sea sector of the West Antarctic Ice Sheet since the Last Glacial Maximum. Quat Sci Rev. 2014; 100:55–86.
22. Broecker, WS., Peng, TH. Tracers in the Sea. Lamont Doherty Geol. Obs. Publ., Columbia University; New York: 1982. p. 689
23. Mackensen, A., Licari, L. Carbon isotopes of live benthic foraminifera from the eastern South Atlantic Ocean: sensitivity to bottom water carbonate saturation state and organic matter rain rates. The South Atlantic in the Late Quaternary – Reconstruction of Material Budget and Current Systems. Wefer, G.Mulitza, S., Ratmeyer, V., editors. Springer; Berlin-Heidelberg: 2004. p. 623-644.
24. Mackensen A. Strong thermodynamic imprint on recent bottom-water and epibenthic $\delta^{13}C$ in the Weddell Sea revealed: Implications for glacial Southern Ocean ventilation. Earth Planet Sci Lett. 2012; 317–318:20–26.
25. Mackensen A, Rudolph M, Kuhn G. Late Pleistocene deep-water circulation in the subantarctic eastern Atlantic. Global Planet Change. 2001; 30:197–229.
26. Hodell DA, Venz KA, Charles CD, Ninnemann US. Pleistocene vertical carbon isotope and carbonate gradients in the South Atlantic sector of the Southern Ocean. Geochem Geophys Geosyst. 2003; 4:1004.doi: 10.1029/2002GC000367
27. Charles, CD., Fairbanks, RA. Glacial to interglacial changes in the isotopic gradients of Southern Ocean surface water. The geological history of the polar oceans: Arctic versus Antarctic. Bleil, U., Thiede, J., editors. Kluwer Academic; Norwell MA: 1990. p. 519-538.
28. Kohfeld KE, Anderson RF, Lynch-Stieglitz J. Carbon isotopic disequilibrium in polar planktonic foraminifera and its impact on modern and Last Glacial Maximum reconstructions. Paleoceanography. 2000; 15:53–64.
29. Bonn W, Gingele FX, Grobe H, Mackensen A, Fütterer DK. Palaeoproductivity at the Antarctic continental margin: opal and barium records for the last 400 ka. Palaeogeogr Palaeoclimatol Palaeoecol. 1998; 139:195–211.
30. Kirshner AE, et al. Post-LGM deglaciation in Pine Island Bay, West Antarctica. Quat Sci Rev. 2012; 38:11–26.
31. Johnson JS, et al. Rapid thinning of Pine Island Glacier in the Early Holocene. Science. 2014; 343:999–1001. [PubMed: 24557837]
32. Mackensen A. Oxygen and carbon stable isotope tracers of Weddell Sea water masses: new data and some paleoceanographic implications. Deep-Sea Res I. 2001; 48:1401–1422.
33. Ishman SE, Szymcek P. Foraminiferal distributions in the former Larsen-A Ice Shelf and Prince Gustav Channel region, eastern Antarctic Peninsula margin: A baseline for Holocene paleoenvironmental change. Antarctic Res Ser. 2003; 79:239–260.
34. Barrett PJ, et al. Oceanography and sedimentation beneath the McMurdo Ice Shelf in Windless Bight, Antarctica. Antarctic Data Series. 2007; 25:95.
35. Ishman, SE., et al. Stable isotopic and foraminiferal evidence of Larsen-B Ice Shelf stability throughout the Holocene. In: Cooper, AK.Raymond, CR., et al., editors. USGS Open-File Rep; Online Proceedings of the 10th ISAES X; 2007. p. 4Ext. Abstr. 018
36. Pudsey CJ, Murray JW, Appleby P, Evans J. Ice shelf history from petrographic and foraminiferal evidence, Northeast Antarctic Peninsula. Quat Sci Rev. 2006; 25:2357–2379.
37. Melis R, Salvi G. Late Quaternary foraminiferal assemblages from western Ross Sea (Antarctica) in relation to the main glacial and marine lithofacies. Marine Micropal. 2009; 70:39–53.
38. Kilfeather AA, et al. Ice-stream retreat and ice-shelf history in Marguerite Trough, Antarctic Peninsula: Sedimentological and foraminiferal signatures. Geol Soc Am Bull. 2011; 123:997–1015.
39. Peck VL, Allen CS, Kender S, McClymont EL, Hodgson DA. Oceanographic variability on the West Antarctic Peninsula during the Holocene and the influence of upper circumpolar deep water. Quat Sci Rev. 2015; 119:54–65.
40. Domack E, et al. Stability of the Larsen B ice shelf on the Antarctic Peninsula during the Holocene epoch. Nature. 2005; 436:681–685. [PubMed: 16079842]

41. Berberich D. Die planktische Foraminifere *Neogloboquadrina pachyderma* (Ehrenberg) im Weddellmeer, Antarktis. Repts Polar Res. 1996; 195:193.
42. Blanchon P, Eisenhauer A, Fietzke J, Liebetrau V. Rapid sea-level rise and reef back-stepping at the close of the last interglacial highstand. Nature. 2009; 458:881–884. [PubMed: 19370032]
43. Whitehouse PL, Bentley MJ, Milne GA, King MA, Thomas ID. A new glacial isostatic adjustment model for Antarctica: calibrated and tested using observations of relative sea-level change and present-day uplift rates. Geophys J Int. 2012; 190:1464–1482.
44. Nicholls KW, Makinson K, Østerhus S. Circulation and water masses beneath the northern Ronne Ice Shelf, Antarctica. J Geophys Res. 2004; 109:C12017.
45. McGlone MS, Turney CSM, Wilmshurst JM, Renwick J, Pahnke K. Divergent trends in land and ocean temperature in the Southern Ocean over the past 18,000 years. Nature Geosci. 2010; 3:622–626.
46. Shevenell AE, Ingalls AE, Domack EW, Kelly C. Holocene Southern Ocean surface temperature variability west of the Antarctic Peninsula. Nature. 2011; 470:250–254. [PubMed: 21307939]
47. Toscano MA, Peltier WR, Drummond R. ICE-5G and ICE-6G models of postglacial relative sea-level history applied to the Holocene coral reef record of northeastern St Croix, U.S.V.I.: Investigating the influence of rotational feedback on GIA processes at tropical latitudes. Quat Sci Rev. 2011; 30:3032–3042.
48. Koffman BG, et al. Centennial-scale variability of the Southern Hemisphere westerly wind belt in the eastern Pacific over the past two millennia. Clim Past. 2014; 10:1125–1144.
49. Dixon DA, et al. An ice-core proxy for northerly air mass incursions into West Antarctica. Int J Climatol. 2012; 32:1455–1465.
50. Smith JA, et al. Sub-ice-shelf sediments record history of twentieth-century retreat of Pine Island Glacier. Nature. 2017; 541:77–80. [PubMed: 27880756]
51. Gohl K. The expedition of the Research Vessel “Polarstern” to the Amundsen Sea, Antarctica. 2010 (ANT-XXVI/3). Repts Polar Mar Res. 2010; 617:173.
52. Gohl K. The expedition ANT-XXIII/4 of the research vessel Polarstern in 2006. Repts Polar Mar Res. 2007; 557:166.
53. Smith JA, et al. New constraints on the timing of West Antarctic Ice Sheet retreat in the eastern Amundsen Sea since the Last Glacial Maximum. Global Planet Change. 2014; 122:224–237.
54. Stuiver M, Reimer PJ. Extended ^{14}C data base and revised CALIB 3.0 ^{14}C age calibration program. Radiocarbon. 1993; 35:215–230.
55. Reimer PJ, et al. INTCAL13 and MARINE13 radiocarbon age calibration curves 0-50,000 years cal BP. Radiocarbon. 2013; 55:1869–1887.
56. Appleby, PG. Chronostratigraphic techniques in recent sediments. Tracking environmental change using lake sediments. Volume 1: Basin analysis, coring and chronological techniques. Last, WM., Smol, JP., editors. Kluwer Academic; Dordrecht: 2001. p. 171-203.
57. Richter, TO., et al. The Avaatech XRF Core Scanner: technical description and applications to NE Atlantic sediments. New Techniques in Sediment Core Analysis. Rothwell, RG., editor. Vol. 267. The Geological Society of London; London: 2006. p. 39-50.Geol. Soc. London Special Publ
58. Hillenbrand C-D, Kuhn G, Frederichs T. Record of a Mid-Pleistocene depositional anomaly in West Antarctic continental margin sediments: an indicator for ice-sheet collapse? Quat Sci Rev. 2009; 28:1147–1159.
59. Nürnberg CC, Bohrmann G, Schlüter M. Barium accumulation in the Atlantic sector of the Southern Ocean: results from 190.000-year records. Paleoceanography. 1997; 12:594–603.
60. Jaccard SL, et al. Two modes of change in Southern Ocean productivity over the past million years. Science. 2013; 339:1419–1423. [PubMed: 23520109]
61. Weltje GJ, Tjallingii R. Calibration of XRF core scanners for quantitative geochemical logging of sediment cores: Theory and application. Earth Planet Sci Lett. 2008; 274:423–438.
62. Barker S, Greaves M, Elderfield H. A study of cleaning procedures used for foraminiferal Mg/Ca paleothermometry. Geochem Geophys Geosyst. 2003; 4:8407.doi: 10.1029/2003GC000559

63. de Villiers S, Greaves MJ, Elderfield H. An intensity ratio calibration method for the accurate determination of Mg/Ca and Sr/Ca of marine carbonates by ICP-AES. Geochem Geophys Geosyst. 2002; 3 GC000169. doi: 10.1029/2001GC000169
64. Misra S, et al. Determination of B/Ca of natural carbonates by HR-ICP-MS. Geochem Geophys Geosyst. 2014; 15:1617–1628. DOI: 10.1002/2013GC005049
65. Rosenthal Y, et al. Interlaboratory comparison study of Mg/Ca and Sr/Ca measurements in planktonic foraminifera for paleoceanographic research. Geochem Geophys Geosyst. 2004; 5 Q04D09. doi: 10.1029/2003GC000650
66. Greaves M, et al. Interlaboratory comparison study of calibration standards for foraminiferal Mg/Ca thermometry. Geochem Geophys Geosyst. 2008; 9 Q08010. doi: 10.1029/2008GC001974
67. Pena LD, et al. Characterization of contaminant phases in foraminifera carbonates by electron microprobe mapping. Geochem Geophys Geosyst. 2008; 9 Q07012. doi: 10.1029/2008GC002018
68. de Lange GJ, Van Os BJH, Poorter R. Geochemical composition and inferred accretion rates of sediments and manganese nodules from a submarine hill in the Madeira Abyssal Plain, eastern North Atlantic. Mar Geol. 1992; 109:171–194.
69. Hasenfratz AP, et al. Determination of the Mg/Mn ratio in foraminiferal coatings: An approach to correct Mg/Ca temperatures for Mn-rich contaminant phases. Earth Planet Sci Lett. 2017; 457:335–347.
70. Hein, JR., Koschinsky, A. Deep-Ocean Ferromanganese Crusts and Nodules. Treatise on Geochemistry. Scott, SD., editor. Vol. 13. Elsevier; Amsterdam: 2014. p. 273-291.
71. Hein, JR., et al. Cobalt-Rich Ferromanganese Crusts in the Pacific. Handbook of Ore Mineral Deposits. Cronan, DS., editor. CRC Press; Boca Raton-London-New York-Washington D.C.: 1999. p. 239-279.
72. Bolton BR, Exon NF, Ostwald J, Kudrass HR. Geochemistry of ferromanganese crusts and nodules from the South Tasman Rise, southeast of Australia. Mar Geol. 1988; 84:53–80.
73. Rickaby REM, Elderfield H, Roberts N, Hillenbrand C-D, Mackensen A. Evidence for elevated alkalinity in the glacial Southern Ocean. Paleoceanography. 2010; 25 PA1209. doi: 10.1029/2009PA001762
74. Yu J, Foster GL, Elderfield H, Broecker WS, Clark E. An evaluation of benthic foraminiferal B/Ca and $\delta^{11}B$ for deep ocean carbonate ion and pH reconstructions. Earth Planet Sci Lett. 2010; 293:114–120.
75. Elderfield H, et al. Evolution of ocean temperature and ice volume through the Mid-Pleistocene Climate Transition. Science. 2012; 337:704–709. [PubMed: 22879512]
76. Yu J, Elderfield H. Mg/Ca in the benthic foraminifera *Cibicidoides wuellerstorfi* and *Cibicidoides mundulus*: Temperature versus carbonate ion saturation. Earth Planet Sci Lett. 2008; 276:129–139.
77. Yu J, Elderfield H. Benthic foraminiferal B/Ca ratios reflect deep water carbonate saturation state. Earth Planet Sci Lett. 2007; 258:73–86.
78. Broecker WS, Sutherland WS. Distribution of carbonate ion in the deep ocean: Support for a post-Little Ice Age change in Southern Ocean ventilation? Geochem Geophys Geosyst. 2000; 1:1023.doi: 10.1029/2000GC000039
79. Duplessy JC, Roche DM, Kageyama M. The deep ocean during the last interglacial period. Science. 2007; 316:89–91. [PubMed: 17412954]
80. Piotrowski AP, Goldstein SL, Hemming SR, Fairbanks RG. Temporal relationships of carbon cycling and ocean circulation at glacial boundaries. Science. 2005; 307:1933–1938. [PubMed: 15790848]
81. Curry WB, Oppo DW. Glacial water mass geometry and the distribution of $\delta^{13}C$ of ΣCO_2 in the western Atlantic Ocean. Paleoceanography. 2005; 20 PA1017. doi: 10.1029/2004PA001021
82. Poole, C. Did ice shelf cover for inner Pine Island Bay (Amundsen Sea, West Antarctica) persist until the latest Holocene?. MGeol thesis, Department of Geology; University of Leicester, UK: 2012. p. 83
83. Mackensen A, Grobe H, Kuhn G, Fütterer DK. Benthic foraminiferal assemblages from the eastern Weddell Sea between 68 and 73 °S: Distribution, ecology and fossilization potential. Marine Micropal. 1990; 16:241–283.

84. Murray JW, Pudsey CJ. Living (stained) and dead foraminifera from the newly ice-free Larsen Ice Shelf, Weddell Sea, Antarctica: ecology and taphonomy$. Marine Micropal. 2004; 53:67–81.
85. Mikhalevich VI. The general aspects of the distribution of Antarctic foraminifera. Micropaleontology. 2004; 50:179–194.
86. Murray, JW. An Atlas of British Recent Foraminiferids. Heinemann; London: 1971. p. 244
87. Murray JW. Revised taxonomy, an atlas of British Recent foraminiferids. J Micropal. 2000; 19:44.
88. Schweizer M, Pawlowski J, Duijnstee IAP, Kouwenhoven TJ, van der Zwaan GJ. Molecular phylogeny of the foraminiferal genus *Uvigerina* based on ribosomal DNA sequences. Mar Micropal. 2005; 57:51–67.
89. Schweizer M, Jorissen F, Geslin E. Contributions of molecular phylogenetics to foraminiferal taxonomy: General overview and example of *Pseudoeponides falsobeccarii* Rouvillois, 1974. Comptes Rendus Palevol. 2011; 10:95–105.
90. Mackensen A, Schumacher S, Radke J, Schmidt DN. Microhabitat preferences and stable carbon isotopes of endobenthic foraminifera: clue to quantitative reconstruction of oceanic new production? Mar Micropal. 2000; 40:233–258.
91. Randall-Goodwin E, et al. Freshwater distributions and water mass structure in the Amundsen Sea Polynya region, Antarctica. Elem Sci Anth. 2015; 3 000065. doi: 10.12952/journal.elementa.000065
92. Coplen TB, Kendall C, Hopple J. Comparison of stable isotope reference samples. Nature. 1983; 302:236–238.
93. Vilks G. Comparison of *Globorotalia pachyderma* (Ehrenberg) in the water column and sediments of the Canadian Arctic. J Foram Res. 1975; 5:313–325.
94. Bergami C, Capotondi L, Langone L, Giglio F, Ravaioli M. Distribution of living planktonic foraminifera in the Ross Sea and the Pacific sector of the Southern Ocean (Antarctica). Marine Micropal. 2009; 73:37–48.
95. Kohfeld KE, Fairbanks RG, Smith SL, Walsh ID. *Neogloboquadrina pachyderma* (sinistral coiling) as paleoceanographic tracers in polar oceans: Evidence from Northeast Water Polynya plankton tows, sediment traps, and surface sediments. Paleoceanography. 1996; 11:679–699.
96. Schiebel R, Hemleben C. Modern planktic foraminifera. Paläontologische Zeitschrift. 2005; 79:135–148.
97. Henrich R. Eldholm O, Thiede J, Taylor E, et al.Proceedings of the Ocean Drilling Program, Scientific Results. 1989; 104:189–232.

Europe PMC Funders Author Manuscripts

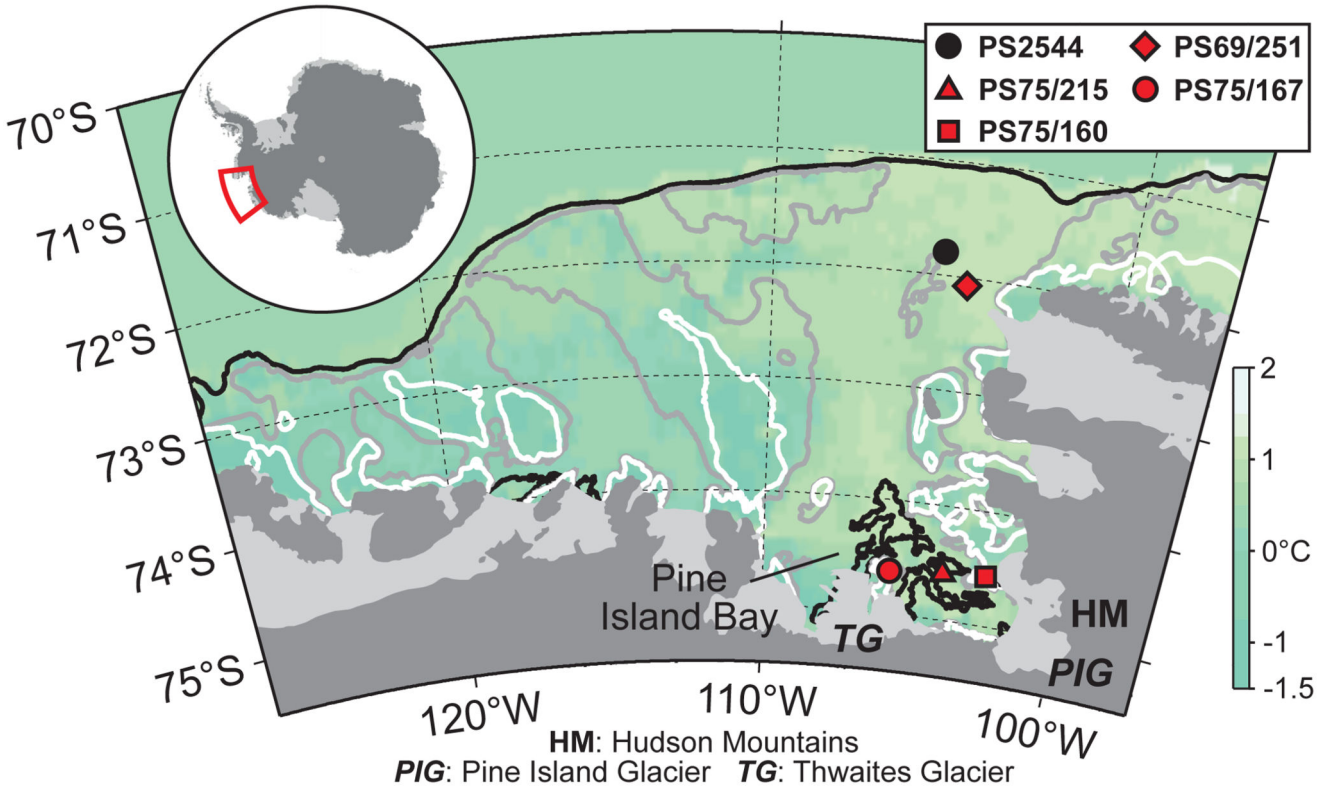

Fig. 1. Map of modern bottom-water temperatures on the Amundsen Sea Embayment shelf.
Red symbols indicate locations of cores analysed in this study, while the black symbol marks the site of a seafloor surface sample investigated for benthic foraminifer $\delta^{13}C$ on *Cibicidoides* spp. by Mackensen24. Bottom-water temperatures (conservative temperatures) are from Schmidtko et al.14. Thick black, grey and white contours indicate seabed elevations of -1000 m, -500 m and -400 m, respectively (for a detailed bathymetric map of inner Pine Island Bay see Fig. 6 in Larter et al.21).

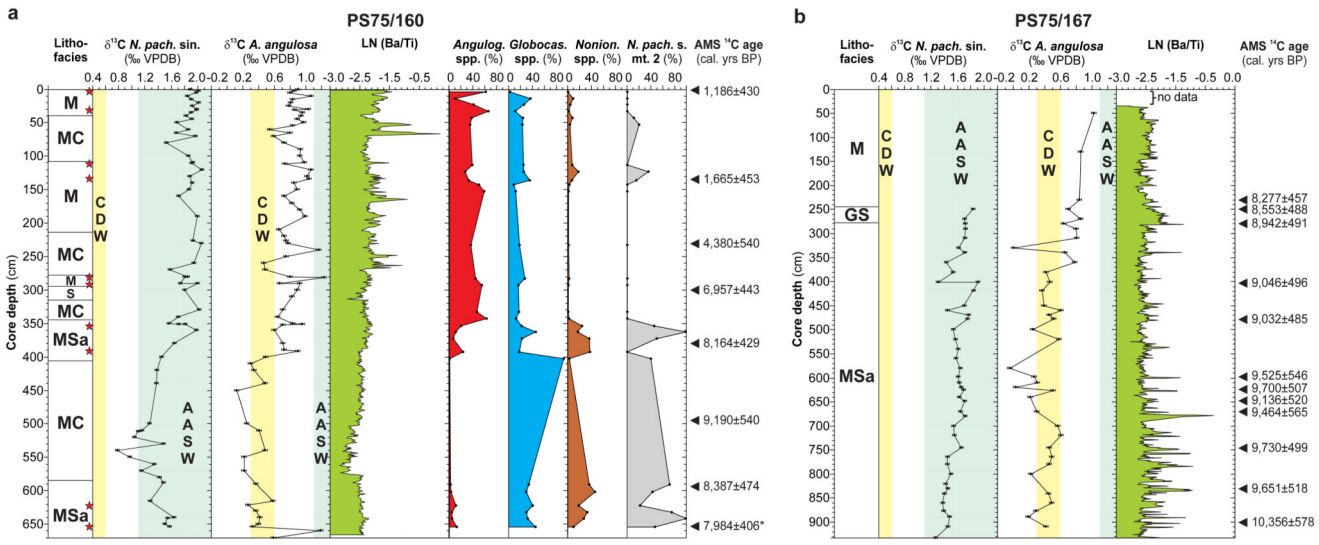

Fig. 2. Proxy data from Holocene marine sediments constraining environmental changes in Pine Island Bay.

Down-core variability of lithological facies, stable carbon ($\delta^{13}C$) isotope composition of foraminifer shells, biological productivity and benthic foraminifer assemblages (core PS75/160 only) is displayed alongside radiocarbon dates for cores PS75/160 (**a**) and PS75/167 (**b**). Lithofacies are from Hillenbrand et al.19 (M: bioturbated mud; MC: deformed, sheared pebble-sized muddy to sandy soft sediment clasts randomly orientated in muddy matrix; MSa: mud interstratified with sandy layers; S: slightly bioturbated sand; GS: massive sandy gravel). AMS ^{14}C dates were recalibrated for this study and are displayed as mean calibrated ages with 2 s.d. error (Extended Data Table 1). Asterisk at lowermost age from core PS75/160 indicates average of replicate dates from the same sample horizon. Facies MC at site PS75/160 probably results from seafloor scouring by iceberg or ice-shelf keels19 but AMS ^{14}C dates indicate reworking only for sediments below ~400 cm depth. The $\delta^{13}C$ values of planktic (*Neogloboquadrina pachyderma* sinistral) and benthic (*Angulogerina angulosa*) foraminifer tests, with error bars illustrating the analytical precision of the measurements, and log-normalised Ba/Ti peak area ratios are shown for both cores. The yellow shaded areas highlight the range of $\delta^{13}C_{DIC}$ values typical for Circumpolar Deep Water (CDW)25,26, while the blue-green shaded areas indicate the $\delta^{13}C_{DIC}$ range typical for Antarctic Surface Water (AASW)32. Abundances of the three main benthic foraminifer groups (*Angulogerina* spp., *Globocassisulina* spp., *Nonionella* spp.) among all benthic foraminifera and of morphotype 2 (mt. 2) shells among all planktic foraminifer shells of *N. pachyderma* sin. (Extended Data Fig. 8) are displayed for core PS75/160. Red asterisks in lithofacies column of core PS75/160 indicate horizons sampled for Mg/Ca analyses on *A. angulosa* (Fig. 3c).

Europe PMC Funders Author Manuscripts

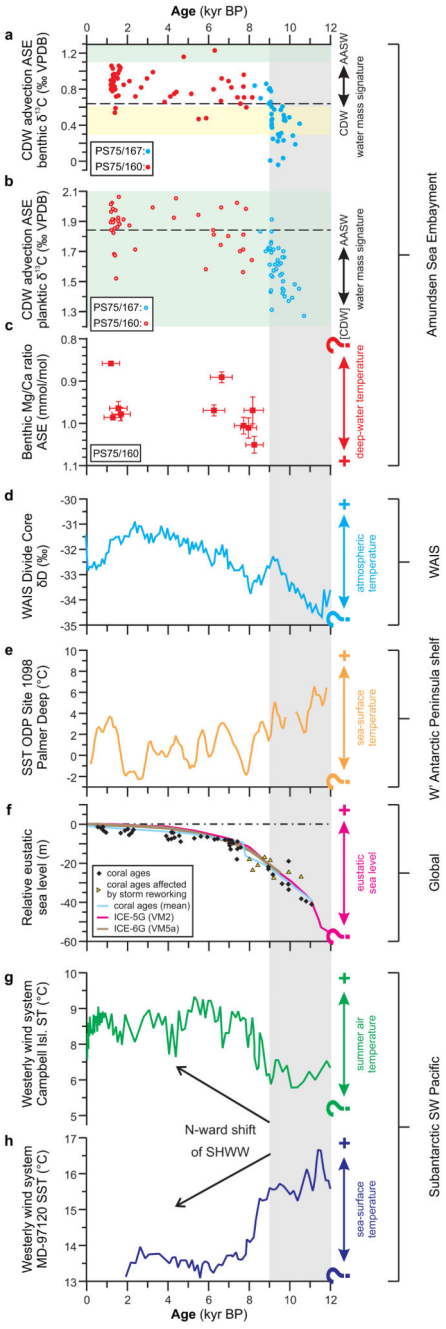

Fig. 3. Variability of Circumpolar Deep Water advection onto the Amundsen Sea Embayment shelf in comparison to potential forcing mechanisms of ice-sheet change in West Antarctica since 12 kyr BP.

Panels (**a**), (**b**) and (**c**): Proxies for CDW advection into Pine Island Bay (PIB). $\delta^{13}C$ values of (**a**) benthic (*A. angulosa*) and (**b**) planktic foraminifera (*N. pachyderma* sin.) in the spliced PS75/160-PS75/167 record, with $\delta^{13}C$ values of modern benthic (PS75/215) and planktic (PS69/251) foraminifera indicated by the black dashed lines and $\delta^{13}C_{DIC}$ ranges typical for CDW and AASW highlighted by the yellow and blue-green shaded areas, respectively; (**c**) Mg/Ca ratios of benthic foraminifera (*A. angulosa*) as a semi-quantitative

proxy for bottom-water temperatures at site PS75/160 (Mg/Ca data corrected for diagenetic coating of shells using Mg/Mn = 0.15 mol mol^{-1} (Methods and Extended Data Fig. 6); ages for Mg/Ca data points were calculated by linear interpolation between maximum and minimum calibrated dates of neighbouring AMS ^{14}C samples (Extended Data Table 1). Panel (**d**): Deuterium (δD) isotope ratio in the WAIS Divide Ice Core from central West Antarctica13 as proxy for air temperature forcing. Panel (**e**): Seawater surface temperature (SST) from ODP Site 1098 in Palmer Deep, western Antarctic Peninsula shelf, as proxy for combined atmospheric and/or oceanic forcing46. Panel (**f**): Sea-level curves42,47 as proxies for sea-level forcing. Panels (**g**) and (**h**): Atmosphere-ocean temperature gradient in the Sub-Antarctic SW Pacific as a proxy for the position of the Southern Hemisphere westerly winds (SHWW)45 (increasing temperature gradient indicates their N-ward shift). (**g**) surface air temperature (ST) on Campbell Island, (**h**) SST at core site MD-97120, SW of New Zealand. Grey shaded area highlights the timing of grounded WAIS retreat from PIB19,21.

Europe PMC Funders Author Manuscripts

Europe PMC Funders Author Manuscripts

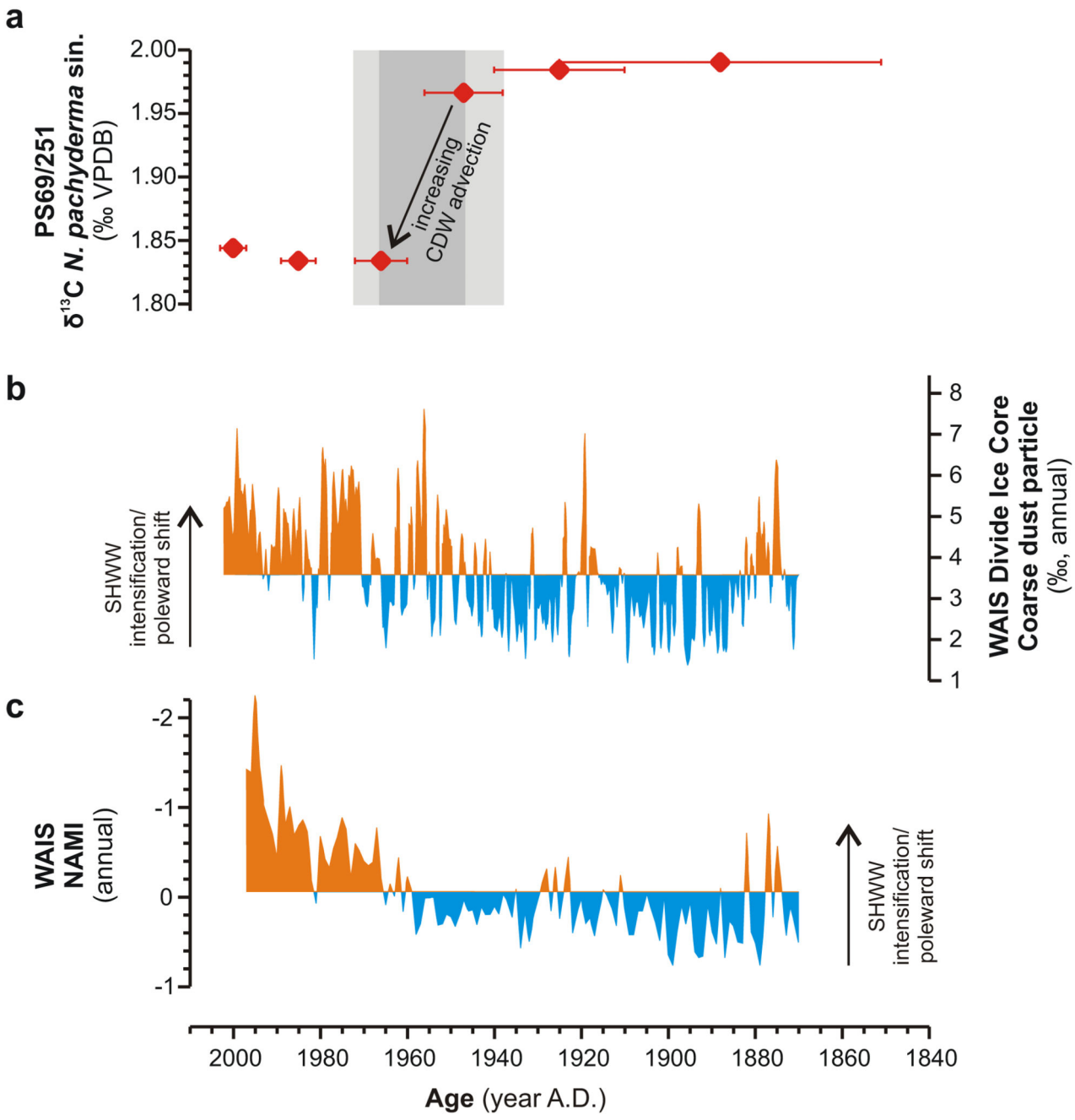

Fig. 4. Variability of Circumpolar Deep Water advection onto the Amundsen Sea shelf and Southern Hemisphere westerly winds during the last 150 years.

Panel (**a**): $\delta^{13}C$ values of planktic foraminifer shells in core PS69/251 from the outer ASE shelf versus age (derived from ^{210}Pb-dating). Error bars of the data points indicate the uncertainty of the ^{210}Pb ages within 1 s.d., and the light and dark grey shaded areas illustrate the possible and most likely timing of an increased admixture of CDW into AASW as indicated by the planktic $\delta^{13}C$ values. Panel (**b**): Annual coarse dust particle percentage (defined as the number of particles mL^{-1} [4.5–15]/[1–15] μm diameter ×100) in the WAIS

Divide Ice Core48. Panel (**c**)**:** Proxy for “northerly air mass incursions” (NAMI) into West Antarctica, based on stacked non-sea-salt Ca^{2+} concentration data from 10 ice cores49. The orange/blue delineation for the curves in panels (**b**) and (**c**) is the mean of that record over the time interval shown. The ice core proxies indicate that intensification and/or poleward shift of the SHWW coincided with increased CDW advection onto the ASE shelf.

Europe PMC Funders Author Manuscripts